2009

An Uhf Frequency-Modulated Continuous Wave Wind Profiler - Development and Initial Results

Iva S. Kostadinova
University of Massachusetts Amherst

AN UHF FREQUENCY-MODULATED CONTINUOUS WAVE WIND PROFILER - DEVELOPMENT AND INITIAL RESULTS

A Thesis Presented

by

IVA KOSTADINOVA

Submitted to the Graduate School of the
University of Massachusetts Amherst in partial fulfillment
of the requirements for the degree of

MASTER OF SCIENCE IN ELECTRICAL AND COMPUTER ENGINEERING

September 2009

Electrical and Computer Engineering

AN UHF FREQUENCY-MODULATED CONTINUOUS WAVE WIND PROFILER - DEVELOPMENT AND INITIAL RESULTS

A Thesis Presented

by

IVA KOSTADINOVA

Approved as to style and content by:

Stephen J. Frasier, Chair

Paul R. Siqueira, Member

Daniel H. Schaubert, Member

Christopher V. Hollot, Department Chair
Electrical and Computer Engineering

To my family, for the way they showed the world to me

The interpretation of our reality through patterns not our own, serves only to make us ever more unknown, ever less free, ever more solitary.

Gabriel Garcia Marquez

ACKNOWLEDGMENTS

At each stage in one's life, there comes this time when the mind is already jumping excitedly from one future life scenario to another, like a bee flying from one flower to the next. But the heart suddenly sits quietly at a corner and tries to capture all that will soon be gone - the quiet summer streets of Amherst, the tasty latte from Amherst Coffee, the view from the top of the LGRT, the moment I got a desk next to a window, the intimidation I felt the first time I walked in MIRSL and the comfort I feel today, the moment I finally called Prof. Frasier just Steve, the magical and impalpable process of building friendships.

I'd like to thank Dr. Frasier for accepting me as his student and giving me the opportunity to peek behind the classroom stage where all the action actually happens. I'd also like to thank Dr. Paul Siqueira for giving me the opportunity to walk in the wild woods of the White Mountains, see a bear, a moose and tell a hemlock from a pine. In the classroom, Dr. Schaubert has helped me climb further up the ladder from where I can now see so much more of the infinite wonders, challenges, and questions in the field of Engineering. For that, and for being an excellent mentor,I extend my respect to him.

Every choice we make is a leap of faith. Choice is in and of itself neither right nor wrong. Often, the circumstances and the people around us can make a choice that seemed wrong, right and vise versa. Many times throughout these two years I felt that my choice to come here was wrong. At the end of this part of my life journey, there is one person who made everything seem right. For his immense patience, caring, love and help, a thousand times, I would make that same choice again. This work wouldn't have come to existence without you!

I always thought that in my thesis acknowledgment (the thesis being this technical document revealing your technical work and skills) I should emphasize on the professional growing I feel I have achieved and acknowledge the people who helped me on the way. But, the truth is that I care the least for my professional achievement and it is the invaluable life experience, and the people who walked with me through it that bring a sense of meaning to it all. Vijay whose heart genuineness cannot be hidden by the constant cigarette smoke around him, Pei whose discipline and professional attitude taught me a lot, Tao who proved to be the best and most entertaining cubicle neighbor, Sumo Tony who walked with me through the "marshes of Harrington" all the way to the other end, Razi who always patiently answered all my quite stupid questions on Linux, Edin whose Bosnian characteristics feel so familiar, Jorge who is a constant source of entertainment even during a serious conversation, Rafael who never said "no", and all the other present lab comrades and the survivors who left just to realize how much stronger they grew in the harsh winters of Amherst and the challenging atmosphere in MIRSL.

For the unconditional love of my family - my mother who shows me how to feel Life, my big brother who never lets go of my hand, my grandmother whose wisdom reveals the beauty of simplicity, and those whose physical presence I can't feel today but whose love reaches me still - my father who taught me about the freedom of mind and my grandparents who gave me a childhood better than a dream, I thank you with all my heart! I dedicate this work to them and hope that they forgive me for all the difficult or happy moments they went through without me.

ABSTRACT

AN UHF FREQUENCY-MODULATED CONTINUOUS WAVE WIND PROFILER - DEVELOPMENT AND INITIAL RESULTS

SEPTEMBER 2009

IVA KOSTADINOVA

M.S.E.C.E., UNIVERSITY OF MASSACHUSETTS AMHERST

Directed by: Professor Stephen J. Frasier

The main challenge in the field of atmospheric boundary layer (ABL) reseach today lies in the need of achieving better temporal and spatial description of its processes. Advancing in that direction means more refined and reliable numerical models for daily weather forcasts, dispersion events, and future global climate on Earth. Microwave radars based on the FMCW technique have proven to be an excellent tool for ABL studies. They provide high sensitivity, high range resolution needed for observation of small scale turbulence, and very small blind range. This thesis describes the ongoing research effort for development of an FMCW wind profiler operating at 915 MHz which at a later stage will utilize spaced antenna (SA) technique for retrieval of 3D winds within the ABL. It discusses in detail the choice of the radar specifications, the hardware development of each of its subsystems, the laboratory tests performed to evaluate their performance, and the results of the first field deployment. Important conclusions and recommendations for the future hardware development of the radar summarize this work.

TABLE OF CONTENTS

LIST OF TABLES

Table **Page**

LIST OF FIGURES

Figure **Page**

CHAPTER 1

INTRODUCTION

1.1 History and Motivation

The processes taking place in the lower troposphere, called atmospheric boundary layer (ABL) have highly influenced life on Earth. Many important weather and climate phenomena are principally driven by the atmosphere-surface interactions in the boundary layer. ABL research and studies help (i) develop and improve the existing numerical weather prediction models, (ii) understand the transfer of heat, water vapor and momentum between the Earth and the atmosphere, (iii) refine the analytical description of turbulent processes, and (iv) quantify the absorption and emission in the troposphere, which is a major factor in shaping climate on Earth. The effect of the troposphere on wave propagation has also been studied extensively for the purposes of improving radio communications. Radio signals are highly sensitive to changes in the refractive index which makes it very important to have a full and detailed description of the refractive index structure, its temporal and spatial variations, and vertical profiles. Radar remote sensing of the troposphere covers a wide range of applications. A major driving force for the fast development of radar technology was the need for continuous monitoring of the wind profiles and fields in the atmosphere. Vertically pointed radars can measure vertical wind velocities. Doppler Beam Swinging (DBS) and Spaced Antenna (SA) techniques are used to retrieve horizontal winds, thus achieving three-dimensional wind fields [17] [16]. The efficient and timely manner of human response to a chemical, biological and nuclear event is primarily based on the accuracy of the dispersion models being developed today. These mod-

els need data from different remote sensing sensors as well as in-situ measurements to estimate the local turbulent intensity and wind fields. Near-surface and low-level winds play a critical role in such estimates. This lower part of the boundary layer is often missed by conventional pulsed radars due to limiting factors such as pulse width and switching speed of the transmit/receive switches when a common antenna is used. Clear air refractive index fluctuations also have a radar cross section (RCS) which can be several orders of magnitude smaller than that of hydrometeors. This leads to high gain and high transmit/receive isolation requirements to achieve the required high sensitivity. Pulsed radars would need fast, high-power switches and good receive/transmit isolation paths.

A frequency-modulated continuous wave radars are a class of radar systems with a 100 (or close to 100) percent duty cycle that utilize a form of frequency modulation on the transmitted signal in order to retrieve range information. Radars based on the FMCW technique have been proven to be an excellent tool in remote sensing of the atmospheric boundary layer. Their strength lies in their high sensitivity due to their high duty cycle and ability to detect refractive index structure parameter C_n^2 with very high spatial and time resolution. Their weakness, on the other hand, are antenna parallax due to the dual antenna system (needed to achieve the required isolation) and uncertainty in the actual sampling volume at near ranges.

The use of FMCW radar for boundary layer research started in the 1960's. Richter [15] was the first to develop and describe the technology in 1969. Almost a decade later Chadwick et al.[5] reported successful Doppler measurements with a FMCW radar. In the following years, observation and further analysis of patterns like Kelvin-Helmholtz instabilities, gravity waves, convection cells, convergence or divergence zones, turbulent plumes, wind shear, jet streams, etc. were strongly facilitated by radar data. FMCW radars were able to provide space and time continuous morphological picture of the boundary layer as well as bulk temperature and pressure information retrieved

from the wind fields [8]. Most of the initial wind profilers operated at the VHF or UHF frequency bands. As reported in [19] there exist few S-band FMCW radars for atmospheric boundary layer studies, one of them being the UMASS S-band FMCW radar developed at MIRSL. The change in frequency band from the more common UHF to S-band alleviates the problem with antenna size but makes the radar sensitive to Rayleigh scattering from insects which can be much greater than the weak Bragg scattering from refractive index irregularities. This requires implementation of effective, and in the case of real time processing, fast DSP techniques that can separate the two effects.

The Microwave Remote Sensing Lab at UMASS, Amherst received an ARO grant "Investigation of Turbulence and Intermittency in the Convective Boundary Layer Using a 915MHz Volume Wind Profiler" (A. Muschinski, S. Frasier, PIs) to develop a low-power, cost effective and mobile UHF FMCW-SA wind profiler that can observe and retrieve information about the structure and processes in the convective boundary layer with high resolution, particularly its lower portion, as well as provide detailed three dimensional wind field measurements. The proposed profiler uses a spaced antenna(SA) technique to retrieve horizontal wind speed instead of the more widely used Doppler Beam Swinging (DBS) technique. Advantages of SA compared to DBS are the reduced time needed for the measurements due to the reduced sampling volume leading to more rapid wind estimates, as well as relaxing the assumption of uniform winds within the volume.

The objective of this thesis is to provide a detailed account of the recent progress achieved in the hardware development of the proposed UHF Wind Profiler. Important design considerations, system integration, and laboratory tests of the radar subsystems account for the main body of this work. First field deployment results, valuable conclusions derived, and recommendations for future work are discussed towards the end.

1.2 Summary of Chapters

Chapter 2 gives a brief description of the atmospheric boundary layer, its structure and characteristics followed by basic clear-air backscattering theory applied to ABL studies with radar remote sensing techniques. At the end of the chapter, the principles of operation of FMCW radars are discussed and important analytical relationships presented. Based on the theory and concepts from Chapter 2, Chapter 3 describes the design and development of the Wind Profiler and its current hardware configuration. A detailed description of the Wind Profiler subsystems - transmitter, receiver, calibration loop, vector modulator section and antennas is given. Chapter 4 presents the laboratory evaluation of the Wind Profiler in terms of its gain, noise figure, sensitivity, calibration, and antenna leakage cancellation. Chapter 5 describes the first field deployments, presents the results and important conclusions derived from them. Chapter 6 contains a summary of the research work presented here, conclusions drawn and recommendations for future work.

CHAPTER 2

FM-CW RADAR PRINCIPLES

FMCW radars have been known as a remote sensing tool for probing clear air atmosphere since the 1970s [15][5]. Some of their major advantages compared to conventional pulsed radars are (i) very high resolution that can reveal small scale turbulence patterns, (ii) small peak to average power ($\approx 100\%$ duty cycle), and (iii) a small blind range that allows for sounding of the lower few hundred meters of the boundary layer. This chapter provides a basic description of the atmospheric boundary layer, derives the relationship between radar parameters and measured physical quantities, and describes the basics of the FM-CW theory of operation.

2.1 Atmospheric Boundary Layer - Definition and Characteristics

The Atmospheric Boundary Layer (ABL) is usually described as the lowest portion of the troposphere where air-surface exchange of heat, moisture, and momentum takes place creating strong mixing and turbulent processes on short time-scales (up to a few hours). The structure and height of the boundary layer exhibit strong diurnal dependence and are highly influenced by the properties of the earth's surface and the processes in the free atmosphere above. Two principle types of boundary layers exist: (i) the convective boundary layer (CBL), where heat from the surface of the Earth creates positive buoyancy flux and instabilities that lead to turbulence, and (ii) stably stratified nocturnal boundary layer (NBL), where negative buoyancy flux decreases the turbulence and stable stratified conditions prevail. During daytime at

mid-latitudes the ABL can reach up to more than 2 km and its usual height at night is between 50 m to 300 m.

The typical structure of the boundary layer is depicted on Figure 2.1 [20]. The surface layer consists of the lowest 10% of the boundary layer where the velocity gradients are higher due to the proximity of the earth surface. This is where buoyancy and turbulence start. On top lays the mixing layer, usually referred to as the convective boundary layer, where air parcels and plumes dissipate their energy while rising until thermal equilibrium is reached. The height of the boundary layer is determined by (i) free atmosphere wind speed, (ii) buoyancy, (iii) free atmosphere density stratification and (iv) free atmopshere vertical wind shear. The top of the boundary layer is called the entrainment zone or capping inversion layer.

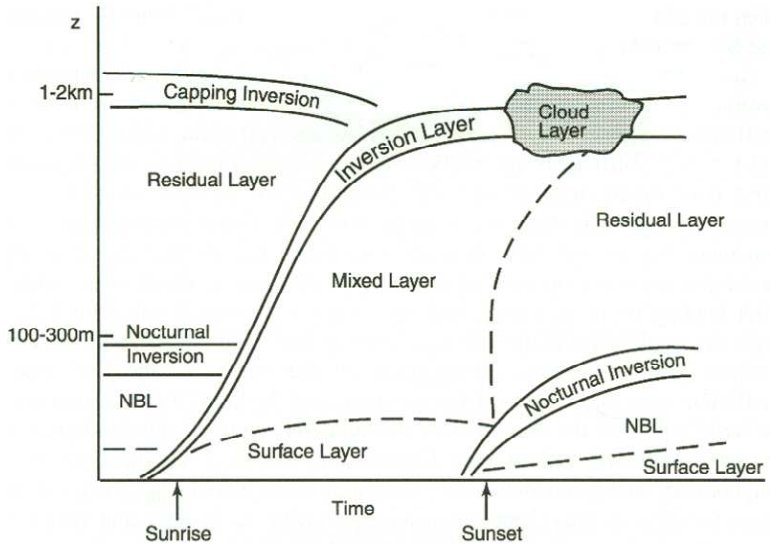

Figure 2.1. Diurnal structure of the boundary layer over land (from Wyngaard, 1992)

2.2 Clear air backscattering theory

In 1966 Hardy and Atlas were the first to attribute the detected backscattered signals from clear air due to Bragg scattering from random fluctuations in the re-

fractive index [8]. According to Bragg's theory, within a given volume of refractive index inhomogeneities, the scattering will be dominated by those inhomogeneities with scales near $L = \frac{\lambda}{2\sin\left(\frac{\theta}{2}\right)}$ where, λ is the radar wavelength and θ is the angle between the incident and scattering directions (equal to 180 degrees for backscatter). Radar backscatter in that sense is equivalent to narrow band filtering of the space spectrum of the refractive index fluctuations.

A good estimate of the intensity of fluctuations for random processes caused by turbulence is the structure function. The structure function of a variable X, where X could be temperature, refractive index or humidity, at point r is defined as [18]

$$D_x(r,d) = E[(X(r+d) - X(r))^2], \tag{2.1}$$

where d is the seperation between the two observed points. For an isotropic and homogeneous turbulence, the structure function of the refractive index becomes dependent only on the separation d and is given by

$$D_n(d) = C_n^2 d^{\frac{2}{3}}. \tag{2.2}$$

The parameter C_n^2 is called the structure constant and is a major characteristic describing the intensity of atmospheric turbulence. The value of C_n^2 can vary from 10^{-12} for strong turbulence to 10^{-17} for very weak turbulence.

To retrieve that spatial turbulent characteristics from time series measurements at a fixed location the theory applies Taylor hypothesis using

$$kS(k) = fS(f), f = uk. \tag{2.3}$$

Here $S(k)$ is the spatial spectrum, k is the spatial wavenumber, $S(f)$ is the temporal spectrum, and u is the mean wind velocity. In his article from 1969, Ottersten [12]

was the first to derive the widely used relationship between radar volume reflectivity and refractive index structure parameter C_n^2 as

$$\eta(\lambda) \approx 0.38 C_n^2 \lambda^{-\frac{1}{3}}. \tag{2.4}$$

In 1941 Kolmogorov developed expression for the energy spectrum of an isotropic, homogeneous and statistically stationary turbulence [21]. The relationship derived by Ottersten is valid within the so called inertial subrange of the Kolmogorov spectrum which extends from scales of a few millimeters to tens of meters within the boundary layer [6]. The radar operating frequency should be chosen such that it falls within that region.

Radar backscatter can also originate through Rayleigh scattering mechanism from birds, insects, and hydrometeors where the size of the scatterers is much smaller than the radar wavelength. This type of backscatter is strongly frequency dependent with the received power being proportional to λ^{-4}. In this case the radar reflectivity is given by [10]

$$\eta = \frac{\pi^5}{\lambda^4} |K|^2 Z \sin^2 \chi, \tag{2.5}$$

where $|K|^2 \approx 0.9$ for microwave frequencies, Z is the reflectivity factor, and χ is the angle between the incident and scattered electric field.

Radar backscatter from birds and insects provides data for studying bird migration patterns and population size. For our purposes, we will look at it as a source of noise contaminating the much smaller backscattered signal from refractive index irregularities.

2.3 FMCW radar theory of operation

The transmitted signal in an FM-CW system is a long, coded waveform of bandwidth B transmitted over a time period T_p, called sweep time. The duty cycle of

such radars approaches 100% and the most commonly used frequency coding is a linear frequency modulation over the bandwidth B. The backscattered signal from an atmospheric target, usually referred to as an echo is a delayed (by the round-trip time to target), attenuated, and possibly Doppler-shifted version of the transmitted waveform. In the receiver, a portion of the transmitted signal is mixed with the echo to produce an intermediate frequency signal. For a point target this is a sinusoidal signal of some frequency called the beat frequency. This beat frequency carries information about the range to the target. For stationary targets, it is related to chirp bandwidth and sweep time as

$$R = \frac{cT_p}{2B} f_b \tag{2.6}$$

where $f_b = \frac{B}{T_p} t$ is the beat frequency, and c is the speed of light.

Figure 2.2 depicts the basics of an FMCW operation. Since there are returns from many targets within the resolution volume the resulting received signal is a superposition of individual sinusoidal signals of varying amplitudes and arbitrary relative phases. Fourier analysis is performed on the received signal and the frequency information is then converted to range.

In an FMCW radar, range resolution means the ability to separate adjacent spectra as shown in Figure 2.2. The frequency resolution in this case is defined as $\Delta f = \frac{1}{T_p}$. As in pulsed radar, the range resolution of an FM-CW system is dependent only on the bandwidth of the transmitted signal. Using Equation 2.6 the range resolution is derived as

$$\Delta R = \frac{cT_p}{2B} \Delta f = \frac{c}{2B}. \tag{2.7}$$

The sampling frequency of the analog to digital (A/D) conversion determines the maximum beat frequency that can be detected without aliasing. The latter determines the maximum range for FMCW radars as

$$R_{max} = \frac{cT_p}{2B} f_{bmax} = \frac{cT_p}{2B} \frac{f_s}{2}. \tag{2.8}$$

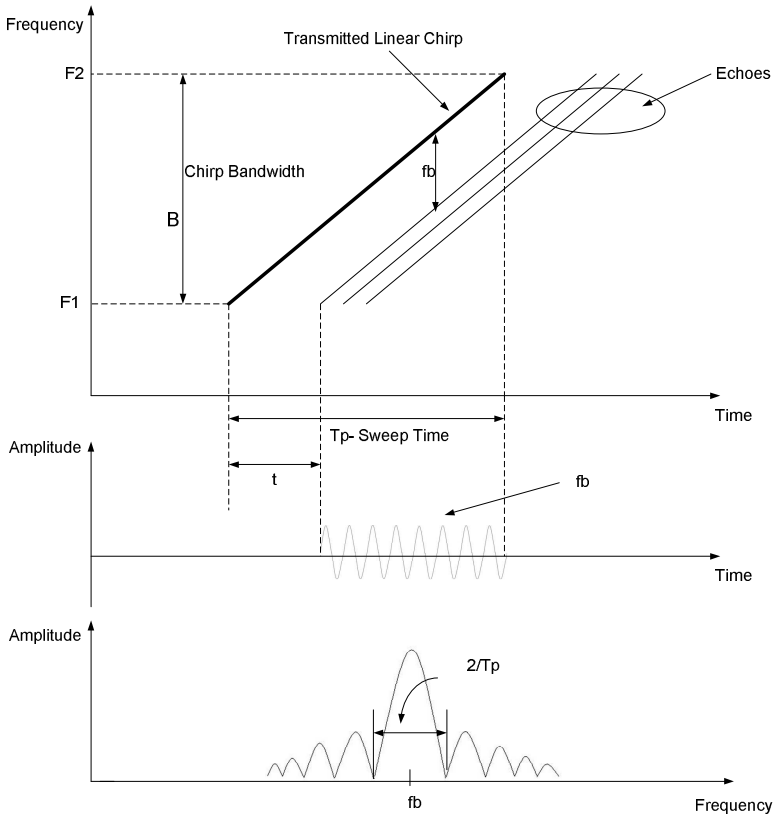

Figure 2.2. FMCW principles

By varying the sweep time T_p and the bandwidth B, the radar can be operated in a mode suitable for particular atmospheric conditions. For example, to improve range resolution the chirp bandwidth B should be increased. Keeping all other parameters the same, this will reduce the maximum range. The maximum unambiguous Doppler velocity in this case will remain the same. If higher unambiguous velocities are desired (see discussion in the next section), T_p should be decreased keeping B the same. This will not affect the range resolution but it will again decrease the maximum range. One of the advantages of FMCW radars is that they allow for change in range resolution without change in the peak transmit power for a given sensitivity.

2.3.1 Doppler measurement and misregistration

The pulse-pair technique may be used as discussed by Chadwick at al. [5] to retrieve Doppler information. Using this techinique, the change in phase of the received signals from two consecutive sweeps carries information about Doppler velocities. For FMCW radars with a duty cycle less than 100% a distinction should be made between the sweep time T_p and the slightly longer pulse repetition period (PRT) T. For a sequence of N uniformly spaced sweeps, the auto-correlation with a time lag equal to the PRT is given by [14]

$$\widehat{R}(T) = \frac{1}{N}\sum_{n=1}^{N-1} V^*(n)V(n+1), \tag{2.9}$$

where $V(n)$ and $V(n+1)$ are the voltage time series of the two consecutive sweeps. The mean Doppler velocity estimate then is

$$\widehat{v} = -\frac{\lambda}{4\pi T}\Phi\left(\widehat{R}(T)\right) \tag{2.10}$$

As seen from 2.10, the Doppler velocity estimates are derived from the received signal sampled with the pulse repetition frequency. In that case, the maximum unambiguous velocity that can be measured is defined by the radar operating frequency, and the pulse repetition frequency f_p as

$$v_{r_{max}} = \frac{\lambda}{4} f_p. \tag{2.11}$$

For moving targets range and Doppler information are coupled in the received signal. If rigorous FM-CW signal analysis is carried out, an expression for the radar

response from a point target at range R_0, moving with radial velocity v_r, (Doppler frequency of f_d) can be derived as [19]

$$y(R) = \frac{\sin\left(\frac{\pi(f_d T_p + (R-R_0))}{\Delta R}\right)}{\frac{\pi(f_d T_p + (R-R_0))}{\Delta R}}, \tag{2.12}$$

where ΔR is the range resolution. Then the apparent range to target is [19]

$$R_{app} = R_0 - f_d T_p \Delta R. \tag{2.13}$$

From (2.13) it is seen that when the target velocity is less than $v_{r_{max}}$, the maximum misregistration is no more than half a range bin. To maximize signal to noise ratio (SNR) it is desirable to make the sweep time T_p long but the length of the sweep is restricted by the coherence of the atmospheric target. The presented theory is based on the assumption that the target remains coherent (i.e. stationary) during the sweep interval and produces a constant-frequency sinusoidal echo [19]. The Doppler spectral width of the echo yields a spread in range through the relationship in Equation 2.13. The rms spread in range is given by [19]

$$\sigma_R = \sigma_f T \Delta R, \tag{2.14}$$

where σ_f is the Doppler spectral width of the echo. To optimize range resolution the sweep time T_p should be equal to σ_f in which case the range spreading is equal to the range resolution.

2.3.2 Radar sensitivity

For bistatic weather radar with Gaussian shaped beams, the received mean power at the antenna port from a scattering volume in the far field is [14]

$$P_r = \frac{P_t G_t G_r \lambda^2 \theta^2 \Delta R \eta}{512 ln2 \pi^2 R^2} C_a, \tag{2.15}$$

where, ΔR - radar range resolution

C_a - antenna correction term

G_t,G_r - transmit and receive antenna gain

λ - radar wavelength

θ - half power beamwidth

η - volume reflectivity

R - range to target.

The parameter C_a accounts for the antenna parallax existing in every bistatic radar and is given by [19]

$$C_a = exp(-2ln2\frac{d^2}{\theta^2 R^2}), \tag{2.16}$$

where d is the distance between the centers of the antennas in meters. Using (2.4), the structure constant can be expressed in terms of the received power as

$$C_n^2 = \frac{P_r 512 ln2 \pi^2 R^2}{P_t G_t G_r 0.38 \lambda^{\frac{5}{3}} \theta^2 \Delta R C_a}. \tag{2.17}$$

The high sensitivity and range resolution in FMCW radars is achieved by pulse compression of the transmitted signal in the receiver. The long transmit pulse produces the high energy needed for good SNR while the pulse modulation provides the desired range resolution [10]. The Wind Profiler uses a linear FM waveform which is the most common because it is easy to generate and high bandwidths can be achieved. Its major disadvantages are the coupling between Doppler and range and pulse envelope weighting (required to reduce range sidelobes) which leads to reduction in SNR.

All pulse compression radars perform some form of matched filtering before detection. In an FMCW radar this filtering, or pulse compression, is obtained by cross-correlation of the transmitted chirp and the received echo, the result of which is constant frequency sinusoid for a point target. Because of the finite observation time,

spectral analysis via DFT compresses this to a sinc function with temporal width of $\tau \approx \frac{1}{B}$ where B is the bandwidth of the chirp. The ratio of the pulse repetition period T and τ is called compression gain and is given by

$$G_c = \frac{T}{\tau} = TB. \tag{2.18}$$

The energy of the pulse stays the same during compression but after correlation it is "compressed" in the main lobe of the sinc function (see Figure 2.2). The power of the signal after compression then can be expressed as

$$P_{comp} = \frac{PT}{\tau} = PTB = PG_c, \tag{2.19}$$

where P is the power of the signal before compression.

The noise power doesn't change during the correlation process since it is not correlated to the transmitted pulse. Thus, the compression gain must be included when evaluating radar sensitivity. For a SNR of unity, using (2.17) we can determine the minimum detectable C_n^2 as

$$C_{n(min)}^2 = \frac{G_c P_n 512 ln2 \pi^2 R^2}{P_t G_t G_r 0.38 \lambda^{\frac{5}{3}} \theta^2 \Delta R C_a}. \tag{2.20}$$

The compression gain can be accounted for by using G_c in the above equation and equivalent system noise $P_n = kT_nBF$, where k is the Boltzman constant, T_n is the antenna temperature (usually observing the cold sky), B is the bandwidth of the transmitted chirp, and F is the noise figure of the receiver. Another way to account for the compression gain is to drop G_c from Equation (2.20), but to reduce B in the system noise equation to the frequency resolution of the sinc function which is equal to $1/T$.

2.3.3 Integration

The minimum detectable C_n^2 can be increased by coherent and/or noncoherent averaging over a period of time thus improving the radar sensitivity. The number of pulses available for coherent integration is closely related to the coherence time of the observed target which is inversely proportional to the Doppler spectral width of its backscatter. It is assumed that during this coherence time, the phase of the target changes much less than a wavelength. Depending on the wavelength and atmospheric conditions the coherence time of an atmospheric target can vary from microseconds to almost a second. The improvement in SNR due to coherent averaging in dB is

$$I = 10\log(N_{coh}), \tag{2.21}$$

where N_{coh} is the number of pulses available for coherent integration. The choice for noncoherently averaged pulses is dictated by the amount of spatial and temporal detail needed in the observed phenomena and the time over which these phenomena don't change significantly over the spatial extent of the resolution volume. The improvement in SNR in dB in this case is

$$I_{ncoh} = 10\log\left(\sqrt{N_{ncoh}}\right), \tag{2.22}$$

where N_{ncoh} is the number of noncoherently averaged pulses.

Averaging is a powerful tool for increasing radar sensitivity and in favourable conditions, wind profilers have been reported to detect echoes with a predetection SNR as small as -30 dB [11].

2.4 Spaced Antenna technique for horizontal wind retrieval

The final design of the UHF FM-CW Wind Profiler will utilize spaced antenna (SA) technique to measure horizontal winds. Currenly, a large percentage of the wind

profilers use the Doppler beam swinging (DBS) technique, where the wind vector is measured in the vertical, and two off-vertical directions to retrieve information about horizontal winds. The DBS technique assumes uniform wind field over the horizontal extend of the beam positions, and over the time needed to swing to all beam directions. SA technique is an alternative to the DBS technique that uses a single vertically directed transmit antenna and three or more spacially separated receive antennas. The reduction of volume that is being sampled relaxes the assumption of uniform horizontal winds. Another advantage of SA technique is that it requires less time for the measurements as only one beam direction is used.

The concept of the SA technique can be explained if a group of targets is considered, advecting along the baseline of the receivers at a single range bin. The mean horizontal wind along the baseline is related to the time lag to the peak of the cross correlation function τ_p of the received voltages at the two receivers, and the distance D between them by [3]

$$v_x = \frac{D}{2\tau_p}. \tag{2.23}$$

This principle was first discussed by Briggs et. al. in the 1950's [3]. They also went on to develop the full correlation analysis (FCA) which uses both the autocorrelation functions and the cross-correlation function between two receivers to retrieve the mean horizontal wind along their baseline. In 1996, Doviak et. al. derived a general form of the auto- and cross- correlation functions for a pair of spaced antennas separated by a distance d_x along the x axis, and d_y along the y axis [7]. The expression takes into account the degradation of the peak of the cross-correlation due to winds perpendicular to the baseline, turbulence, antenna spacing and antenna diameter.-

Two important design considerations are related to the antenna size and spacing. In the presence of turbulence or wind perpendicular to the baseline, the peak of the cross-correlation function degrades (and the auto-correlation function narrows). One

way to alleviate this problem is to use spatial averaging to bring down the variance of the cross-beam winds measured using SA technique. That is why SA techniques usually require relatively wide beams along the direction of separation. For that reason, the Wind Profiler antennas were chosen to have a broad 19° beamwidth. Another configuration that has been used recenly, utilizes a narrow beam transmit antenna and receive antennas that have wide, overlapping beams [16].

In terms of the spacing between the receiving antennas, it is desirable that the spacing is as small as possible (limited by the physical size of the antennas) such that the peak of the cross-correlation function can be well defined. As the antenna spacing is increased the effect of turbulence, perpendicular and/or vertical winds can strongly degrade the cross-correlation making the retrieval of horizontal winds difficult.

In its proposed design the Wind Profiler will use one transmit antenna only and three receive antennas. The received backscatter by the three antennas will be used to estimate cross-beam horizontal winds along the three baselines by applying a full correlation analysis (FCA) or another SA algorithm. The Wind Profiler SA antenna configuration that will be implemented at a later stage is depicted in Figure 2.3.

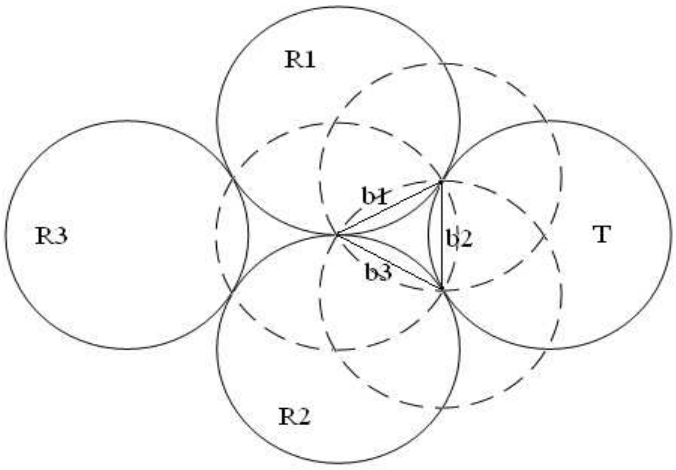

Figure 2.3. Wind Profiler spaced antenna (SA) configuration. T stands for transmit antenna and R1, R2, R3 are the three receive antennas. Solid cicles denote physical apertures, dashed lines denote virtual apertures for SA, and b1, b2, and b3 are the baselines for the SA wind components.

CHAPTER 3

SYSTEM HARDWARE DESCRIPTION

Depending on the desired application, FMCW radars for atmospheric research have different design goals and configurations. This chapter reviews the initial design of the Wind Profiler and the progress done during the last one and a half years, as well as provide a detailed hardware description of the system in its current design stage. Explanation of the particular design choices for the current system configuration and their implications is also presented.

3.1 System Design

3.1.1 Initial Hardware Configuration

The initial Wind Profiler Design started in May 2006 and was conducted by Prof. Stephen Frasier and research engineer Pei-Sang Tsai. Table 3.1 lists the basic system specifications and Figure 3.1 depicts the major blocks of the initial Wind Profiler design.

The Wind Profiler is an FMCW radar that operates in the 900 MHz ISM frequency band (902-928 MHz) with a center frequency of 915 MHz. As mentioned earlier, strong Rayleigh backscatter from insects can contaminated and mask the weak return from refractive index irregularities. When reducing the radar operating frequency from S-band (3GHz) to UHF (915MHz) there is 20.7 dB decrease in the RCS for Rayleigh scatterers of the same size and properties.

The transmitted waveform is a linear FM chirp generated by a Direct Digital Synthesizer (DDS) with a bandwidth of up to 25 MHz giving a maximum range

Parameter	Value
Transmitter	
Center frequency	915MHz
Peak Transmit power	30W
Transmitter type	Solid State RF (SSRF)
Sweep bandwidth	$\leq$25MHz
Sweep time	8.333ms
PRF	100Hz
Receiver	
Noise figure	To be measured
Receiver Gain	74dB
Dynamic range	96dB
Max Range resolution	6m
Antennas	
Type	Four Parabolic dish
Gain	18dB
Polarization	Linear
Front to Back Ratio	22dB

Table 3.1. Initial System specifications

resolution of 6 m. The primary mode of operation is chosen such that the duty cycle of the radar is 83.3% with a chirp length of 8.3333 ms and PRF of 100 Hz, allowing vertical velocity of up to $\pm$8.25 m/s to be resolved with no ambiguity. This makes the radar a powerful tool for vertical wind profiling where turbulent velocities can reach 3-5 m/s. All radar control signals are generated in a Field Programmable Gate Array (FPGA) and are user configurable through the computer serial port (design and implementation done by Albert Genis). Thus, parameters like the PRF and sweep time are variable allowing for change in the maximum unambiguous Doppler velocity without compromising on range resolution. The transmit amplifier is a compact solid state RF power amplifier providing an output power of 30 W.

The receiver chain consists of three identical channels for the three receiving antennas which would allow the SA technique for horizontal wind retrieval to be utilized.

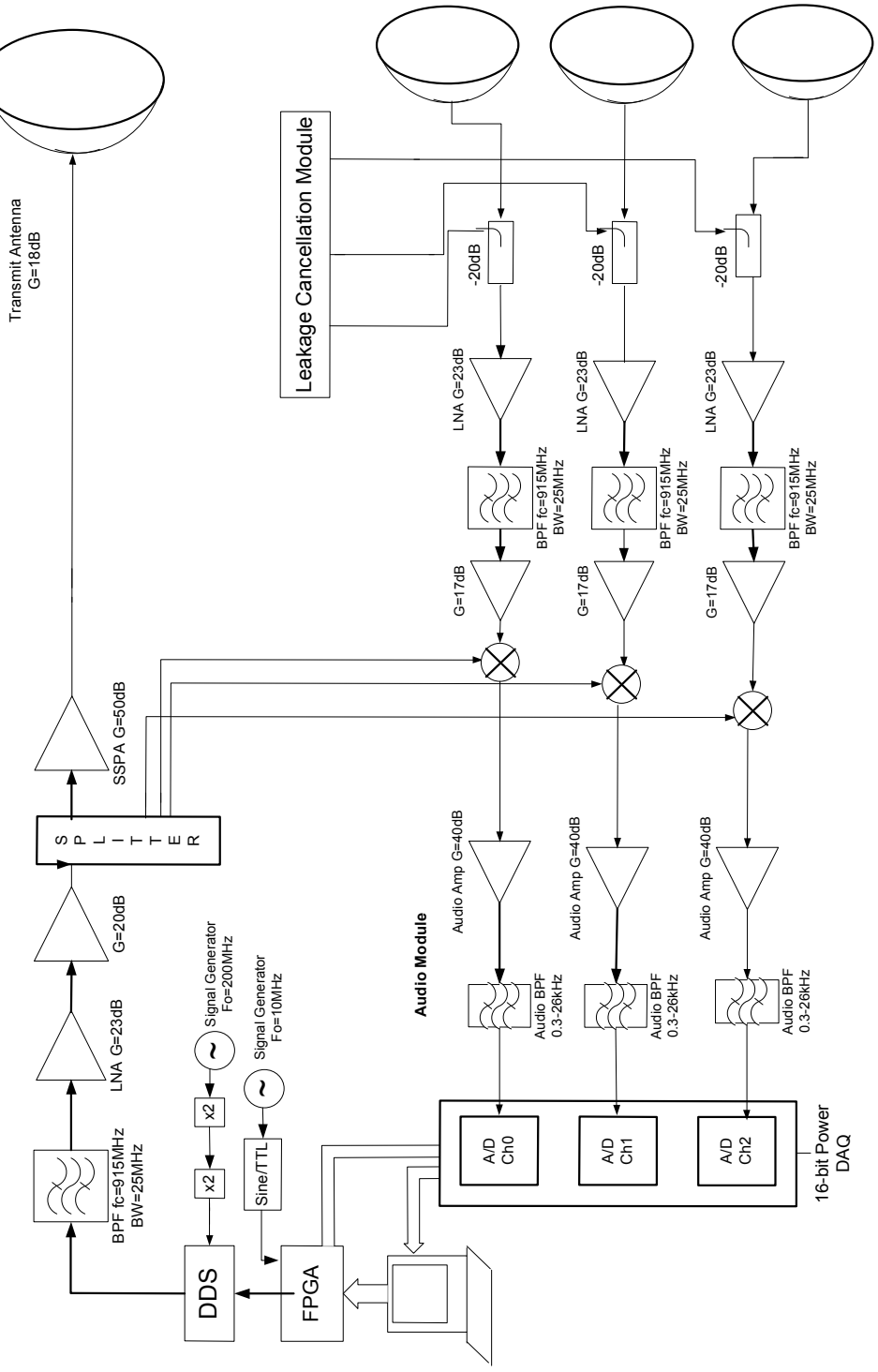

Figure 3.1. Wind Profiler initial configuration

The first component in the receiver chain is a 20 dB coupler followed by a cascade of low noise amplifier, band pass filter, and a 17 dB RF amplifier. The output of the amplifier cascade is passed on to the RF port of the mixer. The IF signal at the mixer output is then fed into the audio module consisting of a bandpass (300 Hz to 26 kHz) filter and a 40 dB voltage gain amplifier. The amplified baseband signal is than sampled by a data acquisition card and stored on a local computer.

The antennas are 1.2 m diameter parabolic dish antennas with dipole antenna feeds, 19 degree beamwidth and gain of 18 dB. The choice of antennas with such a broad beamwidth is required for applying the SA technique and for observations at low altitudes.

Application of the SA technique for horizontal wind retrieval also requires close promixity of the antennas. This affects the isolation between transmit/receive paths and can reduce it to unacceptable levels where the transmit leakage saturates the front end of the receiver. An active cancellation scheme was proposed using a vector modulator to generate a replica of the leaked signal with an opposite phase that would be coupled to the received signal before the low noise amplifier (LNA) in the receiver chain.

3.1.2 Hardware Modifications and Upgrade

The Wind Profiler configuration has undergone a lot of changes in the last year and a half. Table 3.2 list all the changes to the old radar specifications and Figure 3.2 represents the block diagram of the Wind Profiler in its current stage. All blocks that have been added and/or modified in the system are indicated by a different color.

Previously, all power supply components (low-noise linear supplies) were arranged within one enclosure. For better isolation and reducing the ground coupled low-frequency noise, the high power solid state amplifier is now housed in a different enclosure and is powered by a separate A/C power line. The vector modulator can-

Parameter	Value
Transmitter	
Sweep time	Mode 1: 6.25 ms
PRF	Mode 1: 100 Hz
Receiver	
Noise figure	3.1 dB
Receiver Gain	114 dB
Min Detectable Signal	-180 dBm
Antennas	
Antenna Spacing	2.75m
Isolation	$\approx$ 70dB

Table 3.2. Current system specification changes

cellation loop was implemented along with a calibration loop consisting of a 2 μs bulk acoustic wave (BAW) delay line which allows for system calibration and monitoring. A new IF filter was designed and more IF gain added to the system to guarantee that the desired signal power levels are well above the quantization noise floor of the A/D converter.

Prior to modification, the audio module was located in close proximity to the FPGA and the ribbon cables carrying the radar digital control signals were passing right below its terminal board. This caused spurious digital signals to be radiatively coupled to the received signal. The whole audio module is now placed close to the mixer, in a different box, within a solid metal enclosure which significantly reduced all spurious signal interference.

Two antennas - one transmitting and one receiving were mounted on the back of a truck making the whole system mobile and allowing for deployment at multiple locations. Each of the current radar subsystems, as well as the challenges faced during their integration into the Wind Profiler are discussed in greater detail in the following sections.

3.2 Control and Transmit subsystem

The communication between the radar operator and the Wind Profiler is established through a serial interface between the local computer and the Field Programmable Gate Array (Altera Cyclone II EP2C20 FPGA) which generates all radar control signals. The parameters needed for that are stored in a configuration file (fmcw.conf) and can be modified by the radar operator at any time (see Figure 3.3). The initial FPGA design developed by Albert Genis generated all clock signals based on flip-flop counters [2]. The modules generating the different control logic signals did not share a common reference clock signal. That approach is usually inflexible to modification and the design style is often unstable . It also leads to timing skew which is unacceptable for radar systems where synchronization is of utmost importance.

This, and the need for new vector modulator control signals required a completely new design based on synchronous counters. Synchronous counters also utilize flip-flops, but here, each state is clocked simultaneously by a common clock signal. Most hardware-based synchronous counters use logic gates that control the data flow between each state. Synchronous counters can also be implemented using hardware finite state machines which allow for smoother transitions and faster design modification. Currently, all Wind Profiler control signals are generated using a finite state machine. The input to the state machine is controlled by the user through the serial interface and each output state corresponds to a desired control logic signal. This hardware design approach minimizes synchronization problems and makes the addition and/or modification of the control signals easy.

The transmitted chirp is generated by a 10-bit Direct Digital Synthesizer (DDS) from Analog Devices (AD9858). It receives the parameters necessary for frequency sweep generation (see Figure 3.3) from the control subsystem . The board uses an external 800 MHz clock referenced to the 10 MHz FPGA clock.

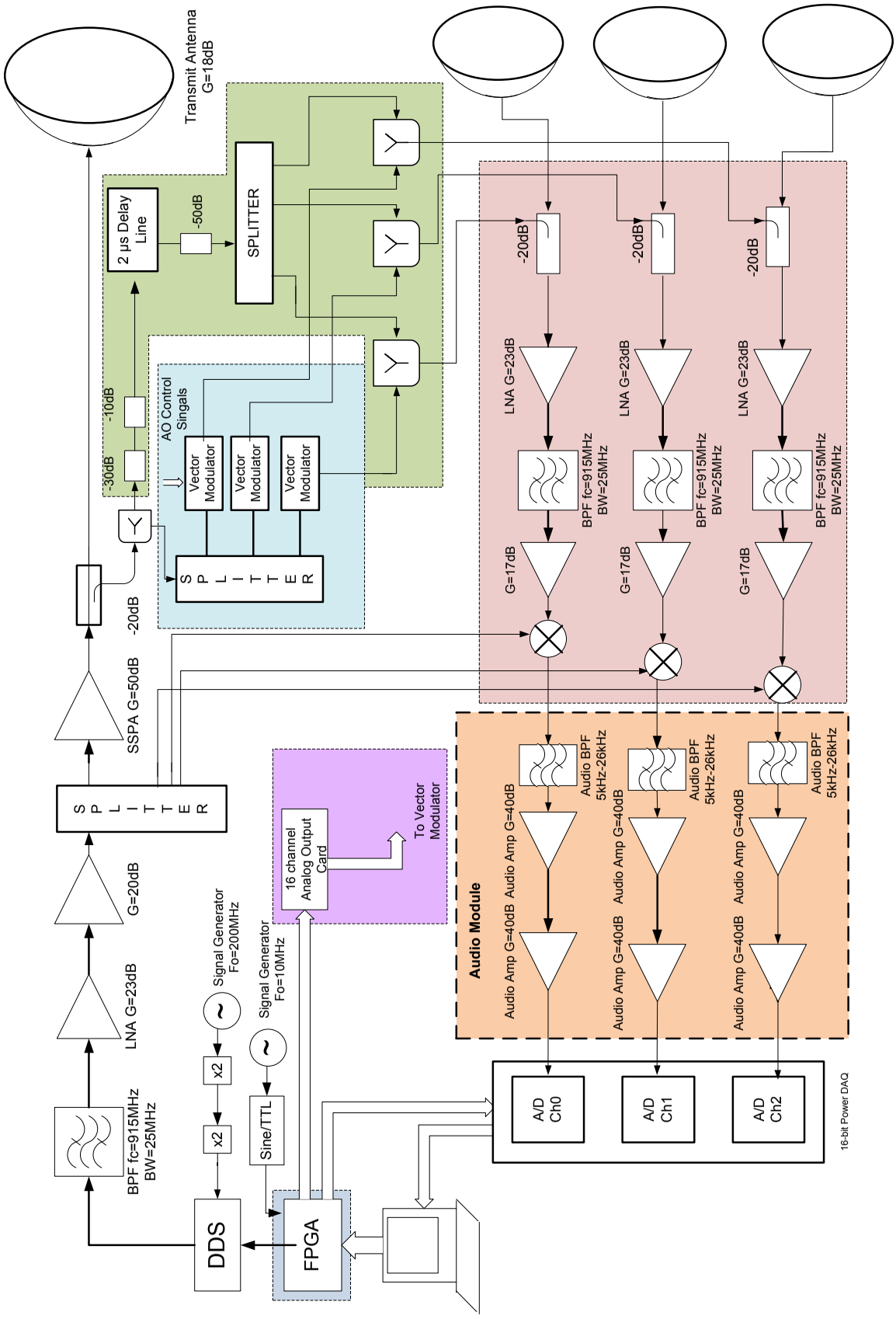

Figure 3.2. UHF FM-CW Wind Profiler block diagram

The internal analog mixer combines the clock signal with the generated chirp centered at 115 MHz to produce the desired product at 915 MHz at the output of the DDS. The undesired mixing products are then filtered, and the signal is passed through a cascade of amplifiers (PA991C with $G = 23$ dB and LNBDA from Wenzel Associates, Inc with $G = 20$ dB) which guarantee the necessary power levels to the mixers in the receiver chain and the solid state RF amplifier. A 4-way splitter is used to split the transmitted signal to the three LO inputs of the mixers and the RF high power amplifier. The high power amplifier is a linear power solid state RF amplifier from OPHIRrf with a gain of 50 dB and a 1 dB compression point set at 30 W (44.8 dBm). The through port of a 20 dB directional coupler delivers the output of the amplifier to the antenna and couples part of it to a 2-way splitter that sends copies of the signal to the calibration and vector modulator loops.

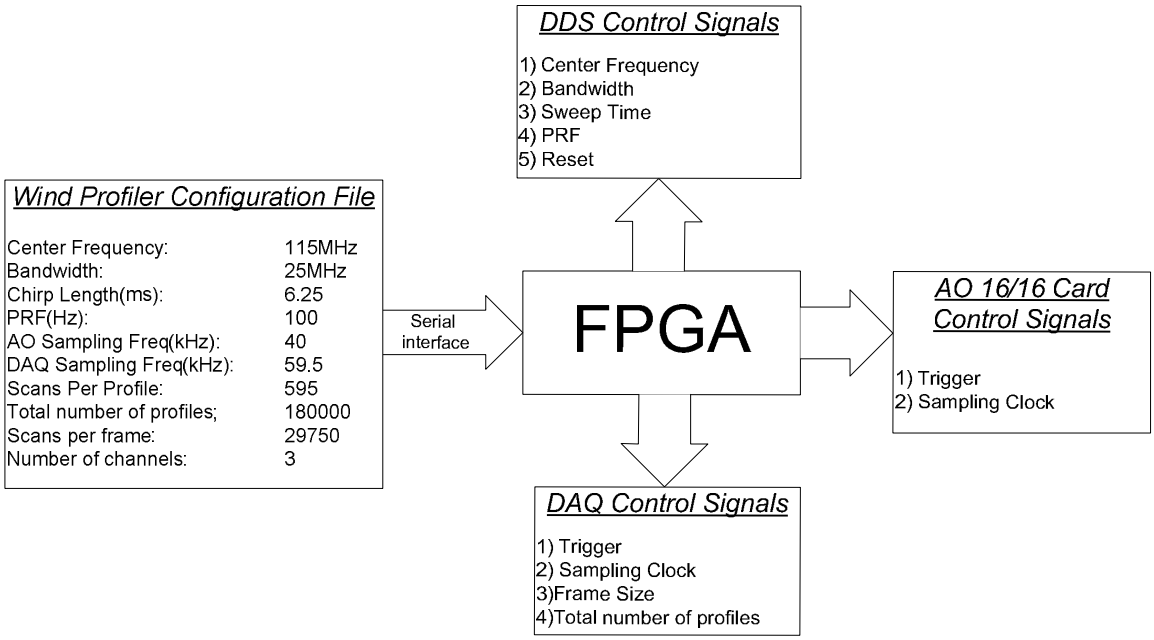

Figure 3.3. FPGA control signals generation

3.3 Calibration Loop

Implementation of a calibration loop in a radar system allows for continuous monitoring of system performance and gives a reference point for evaluating the radar sensitivity. For this purpose, a bulk acoustic wave (BAW) delay line, with an effective delay of 2 μs, was purchased from Teledyne Electronic Technologies. A portion of the transmitted chirp, attenuated to a level that is safe for the device serves as its input. The output of the delay line is further attenuated and combined with the active cancellation signal from the vector modulator (described in the following section) in a power combiner. The output of the combiner is then coupled into the receiver chain through a 20 dB coupler (see Figure 3.2). The delayed chirp produces a signal with a beat frequency f_b at the mixer's IF port. This corresponds to a radar range of 300 m. Some of the important delay line specifications are listed in Table 3.3.

Parameter	**Value**
Center frequency	915 MHz
Bandwidth	25 MHz
Time Delay	$2.000 \pm 0.012 \mu s$
Insertion Loss at 915 MHz	11.5 dB
Triple Travel Suppression	11 dB min
Peak Power	100 mW

Table 3.3. Delay line specifications

One of the important performance characteristics of the delay line is the triple travel signal suppression. To analyse that performance an analytical model for the output signal of the delay line is derived below. That output signal is a summation of the nominal 2 μs delayed chirp and the triple travel chirp and can be expressed as

$$S(t) = (A - B)\sin\left(\frac{2\pi B}{T_p}t^2 + 2\pi f_1 t\right) + B\sin\left(\frac{2\pi B}{T_p}t^2 + 2\pi f_1 t\right)$$

$$+B\sin\left(\frac{2\pi B}{T_p}(t-\tau)^2 + 2\pi f_1(t-\tau)\right), \tag{3.1}$$

where f_1 is the chirp starting frequency and τ is the time delay difference between the nominal and triple travel signal which in the case of this delay line is equal to 4 μs, A is the amplitude of the nominal 2 μs delayed chirp, and B is the amplitude of the triple travel chirp. The worst case suppression for the delay line is specified to be 11 dB, suggesting that B is much smaller than A. Looking only at the last two terms and using a well known trigonometrical identity we get

$$S(t) = B \sin\left(\frac{2\pi B}{T_p}t^2 + 2\pi f_1 t - \frac{2\pi B}{T_p}\tau t\right)\cos\left(\frac{2\pi B}{T_p}\tau t\right). \tag{3.2}$$

The effect on the first term is a shift in the center frequency of the chirp by $\frac{2\pi B}{T_p}\tau$. The second term leads to the chirp being modulated by a sinusoidal signal of frequency $\frac{B\tau}{T_p}$. This modulation can be seen on Figure 3.4 which shows the $S21$ scattering coefficient of the delay line for a small portion of the chirp frequency spectrum between 914 MHz and 916 MHz. The amplitude of that sinusoidal signal carries information about the available triple travel signal supression in the Wind Profiler delay line, which was found to be about 16 dB.

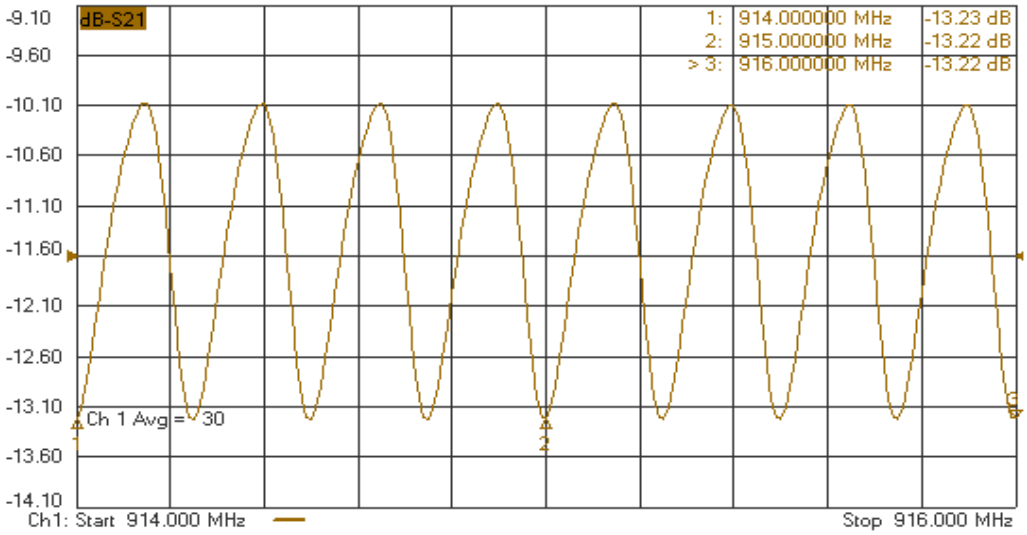

Figure 3.4. Measured delay line insertion loss

The effect of the delay line will be to produce an equivalent of two targets - the first one centered at f_b corresponding to a range at 300 m and another one at 900 m with an equivalent power about 16 dB below the first one.

Considering the equivalent target at 300 m, and using the radar equation, a relationship between the received power through the delay line and its radar reflectivity can be derived as [19]

$$P_{cal} = \frac{P_t G A_{eff} \eta_{cal} \Delta R \pi \theta^2}{(4\pi R)^2 L_{ant} 8ln2} = \frac{P_t}{L_{cal}}, \tag{3.3}$$

where L_{ant} is the total loss in the antenna feedlines, and L_{cal} is the loss through the calibration path. For Gaussian shaped beams, $G\theta^2 = 16ln2$, giving an equivalent volume reflectivity of the calibration target of

$$\eta_{cal} = \frac{8\pi R^2 L_{ant}}{A_{eff} \Delta R L_{cal}}. \tag{3.4}$$

The received reflectivity as a function of distance can be expressed as

$$\eta_r = \frac{P_r \eta_{cal}}{P_{cal}}. \tag{3.5}$$

Using (3.5) in (2.4) the relationship between the received power P_r and the structure constant C_n^2 can be expressed as

$$C_n^2 = \frac{\lambda^{\frac{1}{3}} \eta_r}{0.38} = \frac{\lambda^{\frac{1}{3}} P_r \eta_{cal}}{0.38 P_{cal}}. \tag{3.6}$$

The delay line is also very useful for comparing theoretical and real system performance. Knowing the volume reflectivity of the equivalent target and the measured noise floor of the system, it is immediately known what is the minimum detectable signal for a given SNR.

3.4 Leakage Cancellation Loop

Application of spaced antenna (SA) techniques for horizontal wind retrieval requires antennas with broad beams mounted in close proximity to each other. This can result in inadequate isolation between the transmit and receive antennas such that the transmit leakage saturates the receiver front end. The measured isolation between the Wind Profiler antennas is ≈ 70 dB. The mixer used (see Figure 3.2) is a high power mixer with 1 dB compression point of 9 dBm. For the given isolation it is the first component to saturate in the receiver chain. Hence, active leakage cancellation is required which guarantee the linear operation of the mixer - critical for reliable Doppler measurements. To achieve this goal, a RF vector modulator was purchased from Analog Devices (AD8340). The operation principles of the modulator are depicted in Figure 3.5.

The vector modulator receives a signal at its input which is split into in-phase (I) and quadrature (Q) components. Variable attenuators receive control signals and attenuate the I and Q components relative to each other such that the output signal is a replica of the input with the desired new magnitude and phase. The modulator uses Cartesian single-ended or differential control signals to control the attenuation. For better noise performance, it is recommended to use the vector modulator control inputs in differential mode. The relationship between the desired gain and phase, and the corresponding control signals is

$$Gain = \sqrt{\left(\frac{V_{BBI}}{V_O}\right)^2 + \left(\frac{V_{BBQ}}{V_O}\right)^2}, \tag{3.7}$$

$$Phase = \arctan\left(\frac{V_{BBQ}}{V_{BBI}}\right), \tag{3.8}$$

where $V_O = 500$ mV is the baseband scaling constant and V_{BBI}, V_{BBQ} are the differential I and Q control baseband voltages, respectively. The differential full scale range of V_{BBI} and V_{BBQ} is ± 500 mV. The maximum gain of unity is achieved if the

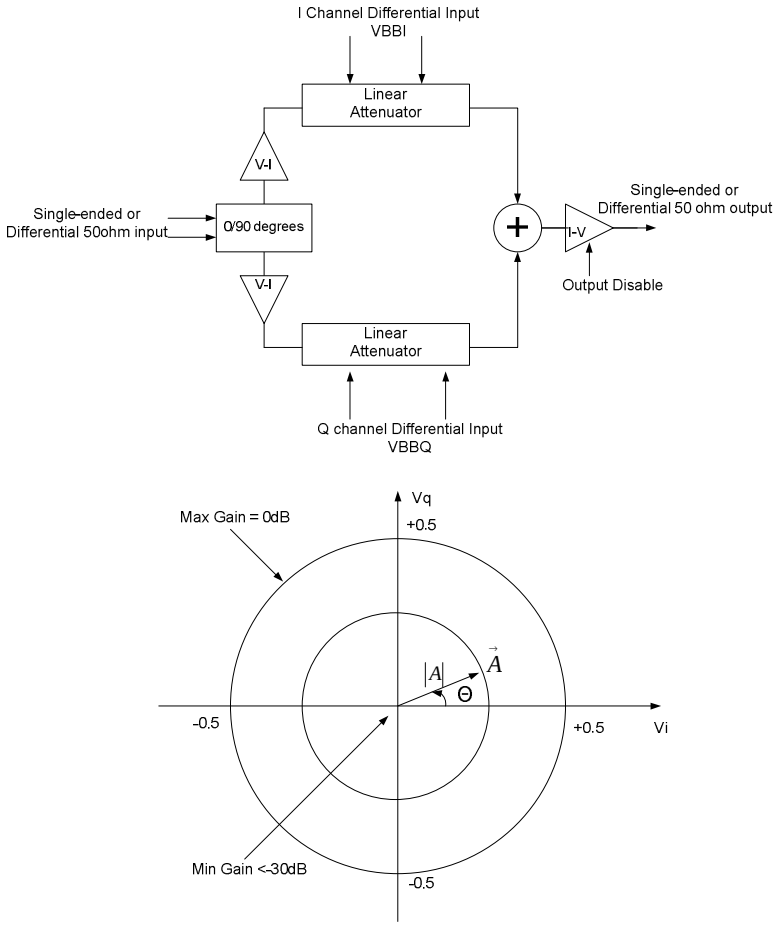

Figure 3.5. Vector modulator block diagram and operating principle

differential voltage is equal to +500 mV or -500 mV. So with a common mode level of 500 mV,V_{BBI} and V_{BBQ} will each swing between 250 mV to 750 mV.

The signal generation and control of the cancellation loop is depicted on Figure 3.6. A software program generates the differential control signals V_{BBI} and V_{BBQ}, and passes these values via a 96-pin cable to a 16-bit 16-channel D/A converter (PD2-AO-16/16 - PCI Analog Output Data Aquisition Board from United Electronic Industries). The trigger and sampling clock for the board are generated in the FPGA and are synchronized with the radar PRF. The analog differential control signals are then delivered to the vector modulator control signal inputs for each of the three channels.

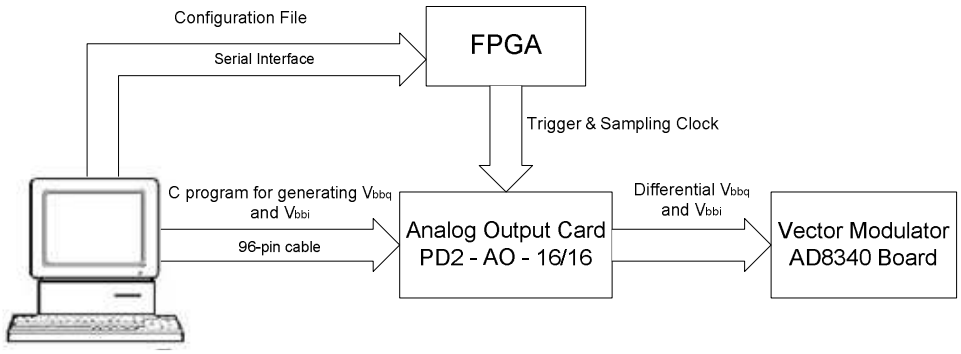

Figure 3.6. Cancellation loop control signals

Figure 3.7 shows the part of the radar block diagram that represents the hardware implementation of the loop. Right before the transmit antenna, part of the transmitted chirp is coupled through a 20 dB coupler into a 2-way splitter that splits it equally to the calibration and cancellation loops. A 3-way splitter delivers the signal to the input of the vector modulator for each channel. Appropriate attenuation is added to ensure that the input level is within the safe operating range of the modulators. The differential control signals from the Analog Output Board are fed into the control signal inputs of the modulator. A total of 6 differential signals are required for the three vector modulators. The control signals are computed such that the output of the vector modulator is a replica of the transmitted chirp that is opposite in phase to the antenna leakage and 20 dB larger than it in magnitude. The first component in the receiver chain after the antenna is a 20 dB coupler used to couple the vector modulator output to the received signal, thus cancelling the leakage and assuring the linear operation of the mixer.

The antenna leakage can be expressed as

$$S(t) = A \sin\left(\alpha t + \beta t^2 + \phi\right), \tag{3.9}$$

where A is the leakage amplitude, $\alpha = 2\pi f_{start}$ and $\beta = \frac{2\pi B}{T_p}$. Depending on the length of the coupling path the leakage is delayed by some time τ relative to the

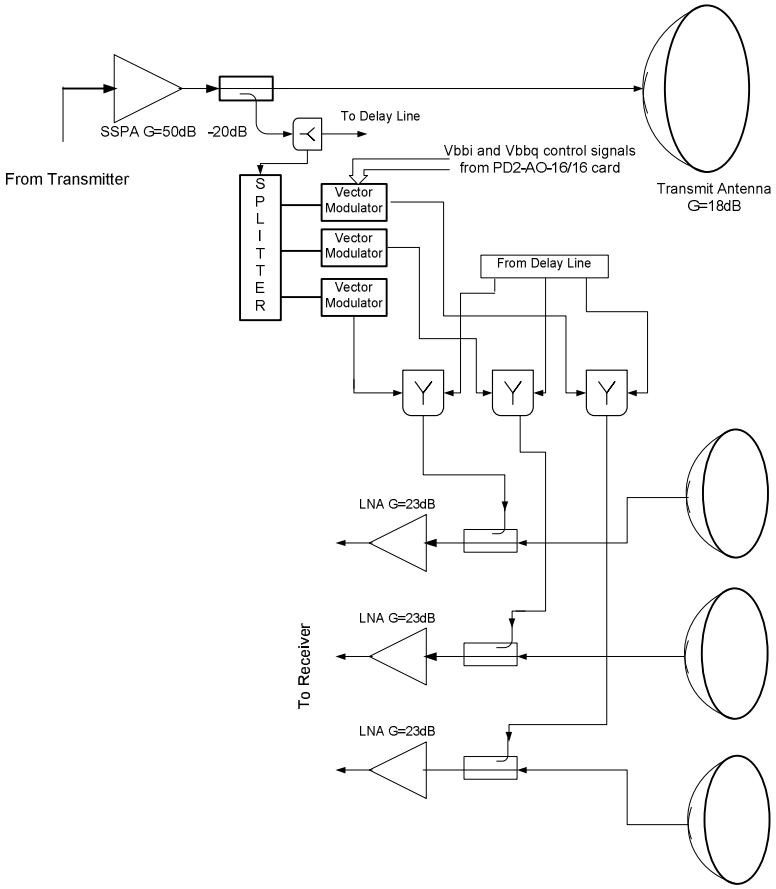

Figure 3.7. Cancellation loop hardware design

vector modulator input. The latter then can be written as

$$V_{in}(t) = B\sin\left(\alpha(t+\tau) + \beta\left(t+\tau\right)^2 + \phi + \phi_0\right), \tag{3.10}$$

where$B$ is the amplitude and ϕ_0 is the phase added by the components on the vector modulator path. For leakage cancellation, the required output of the vector modulator should be

$$V_{out}(t) = A\sin\left(\alpha t + \beta t^2 + \phi + \pi\right). \tag{3.11}$$

Expanding the equation for the vector modulator input we get

$$V_{in}(t) = B\sin\left(\alpha t + \beta t^2 + \phi + \alpha\tau + \beta\tau^2 + \phi_0 + 2\beta\tau t\right). \tag{3.12}$$

The first three terms represent the phase of the leakage. The required phase change in the vector modulator is then given by

$$\Psi(t) = -\left(2\beta\tau t + \alpha t + \beta\tau^2 + \phi_0 - \pi\right). \tag{3.13}$$

It is obvious that the needed phase change is a function of time. This requires precise dymanic control of the vector modulator which has to be synchornized at each chirp to achieve reliable cancellation. Such precision is very hard to achieve. If the input to the vector modulator is delayed by the same time delay, then $\tau = 0$ and the required phase change becomes

$$\Psi = -\phi_0 + \pi. \tag{3.14}$$

Clearly, now the required phase change is independent of time and no dynamic control of the vector modulator is needed. Allignment of the two chirps is achieved by adding the required length of cable at the input of the vector modulator, its length dependent on the length of the antenna feed lines in the particular deployment conditions.

The maximum cancellation that can be achieved depends on (i) how well the leakage and the input to the vector modulator are alligned in time (assuming the delay within the vector modulator itself is insignificant) and (ii) how small the amplitude error between the two signals is. Misallignment in time corresponds to the case where dymanic phase change of the vector modulator input is required. Using a constant phase change control in the vector modulator leads to only particular frequiencies within the chirp being well cancelled while for some other frequencies the two chirps may add constructively (see Figure 3.8). Hence, it is critical that the leakage and the vector modulator input chirps are alligned in time as best as possible.

Amplitude errors between the transmitter leakage and the vector modulator output also deteriorate the cancellation loop performance. To maximize cancellation the

error needs to be as small as possible. The maximum cancellation (see Figure 3.8) that can be achieved is

$$C_{max}, dB = P_{leakage} - P_{min_error}. \tag{3.15}$$

For a desired cancellation, the smaller the power in the leakage is the more rigid the constraints are for the maximum amplitude error that can be tolerated. These errors are due to the inaccuracy of the vector modulator, the instruments used to measure the power levels and in a deployment scenario, the backscattered power from very close targets that superimposes on the leakage.

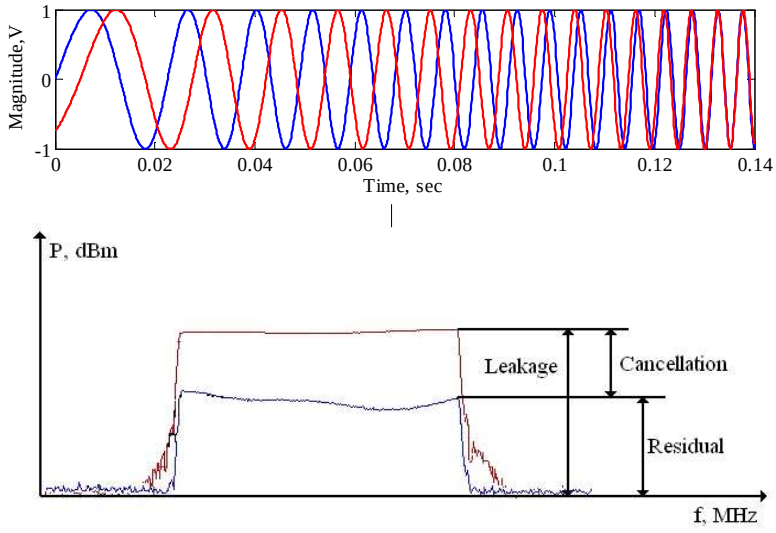

Figure 3.8. Effect of time and amplitude error on the achieved cancellation

3.5 Receiver subsystem - RF section

The receive circuitry consists of three identical RF signal paths for the three receive channels. The received signal is an addition of atmospheric echoes, ground clutter, and transmitter leakage. The leakage, which can be orders of magnitude larger than the echoes, and can easily saturate the front end of the receiver, is cancelled

immediately before the low noise amplifier (LNA) as described in the previous section. The radar calibration signal from the delay line is also coupled into the receiver chain at that point.

The noise figure of the system is primarily determined by the noise figure of the first components in the receiver chain. To ensure a good noise figure, the first component in the receiver is usually a low noise amplifier. In the case of the Wind Profiler, the noise figure of the RF section is given by

$$F_{receiver} \approx L_c + L_c\,(F_{LNA} - 1) + \frac{(L_f - 1)\,L_c}{G_{LNA}} + \frac{(F_{amp} - 1)\,L_f L_c}{G_{LNA}}, \tag{3.16}$$

where L_c is the coupler insertion loss and L_f is the filter insertion loss, F_{LNA} is the LNA noise figure and F_{amp} is the noise figure of the 17 dB amplifier in the RF section.

The attenuation of the antenna feed lines should be added to the noise figure given by (3.16) to give the true receiver noise figure as

$$F_{total} = L_{cable} + F_{receiver} L_{cable}. \tag{3.17}$$

The coupler in the Wind Profiler is a 20 dB coupler from Narda Microwave East with insertion loss of $L_{coupler} = 0.3$ dB. The power level of the delay line signal which is coupled into the receiver through the coupler should be such that no extra thermal noise from the transmitted signal gets coupled into the receiver. The LNA is a Phoenix PA911C with a noise figure of 0.9 dB. The next component in the chain is a ceramic band pass filter (BPF) from Lark Engineering with a bandwidth of 25 MHz and insertion loss of 2.5 dB. The received signal is then amplified again by a 17 dB amplifier from Mini Circuits (ZJL-4HG+) with a noise figure of 5.01 dB before being passed on to the mixer. With the given specification of the components on the RF chain the calculated $F_{receiver}$ is 1.28 dB.

The choice of the mixer is dictated by (i) how strong the transmit leakage is and, (ii) the receiver gain of the RF section. The Wind Profiler utilizes high power mixer from Mini Circuits (ZEM-4300MH+) with a 1 dB compression point of +9 dBm. The mixer has a LO power level of +13 dBm. For reliable performance, the LO level should vary no more than ±3 dB from its specified value. For the Wind Profiler operating frequency range, the mixer insertion loss varies from 6 to 8 dB depending on the LO input level.

3.6 Receiver Subsystem - IF section

The IF section of the receiver in its current stage consist of an audio module (audio filter and a cascade of audio amplifiers) and a data acquisition system.

To determine if the IF gain was adequate, analysis was undertaken to determine if the expected backscattered power from the phenomena desired to be observed utilizes the data acquisition dynamic range. The data acquisition card in the Wind Profiler is a 16-bit PowerDAQ PD2-MFS-4-500/16 from United Electronic Industries, Inc. The specified maximum input voltage is ±10 V corresponding to a maximum power of 30 dBm (monotone). The dynamic range of the DAQ is 96 dB setting its quantization noise floor at -66 dBm. Therefore, to ensure detection of the observed phenomena, the power at the DAQ input should exceed -66 dBm.

Typical values for the structure constant C_n^2 vary from $10^{-15}\ m^{\frac{-2}{3}}$ for weak turbulence to $10^{-13}\ m^{\frac{-2}{3}}$ for intensive turbulence within the convective boundary layer. The received power from refractive index fluctuations at the receiver input can be found using Equation (2.15). Figure 3.9 depicts the mean received power at the receiver input for the different turbulent intensities as well as the data acquisition quantization noise floor referred to the receiver input. In its initial design configuration the Wind Profiler could not detect the desired backscatter and an increase in the receiver gain was needed.

The audio amplifier (VA 1040-2) in the audio module of the receiver is a 40 dB voltage gain amplifier from AVENS Signal Equipment Corp. Another one of the same kind was cascaded with the existing audio module (see Figure 3.2) to bring the total receiver gain to $G = 114$ dB, and the minimum detectable signal at the receiver input to -180 dBm. This ensured that the data acquisition could safely and accurately sample the desired signal.

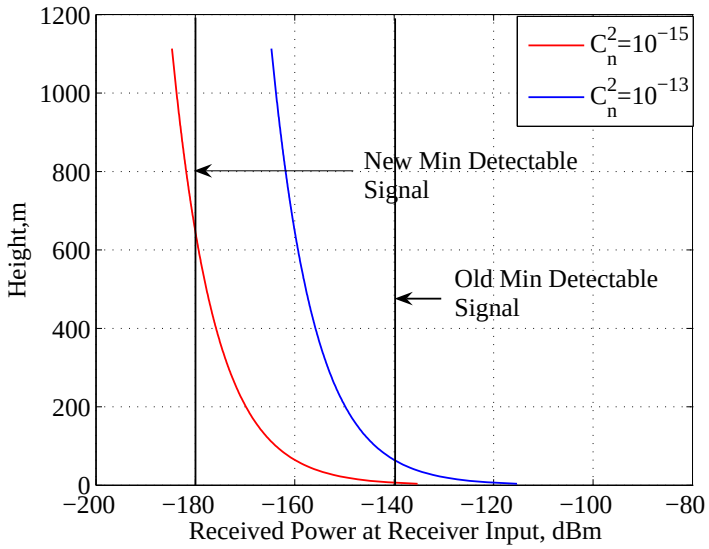

Figure 3.9. Received power and minimum detectable signal

3.6.1 IF Filter Time-Domain Response

The audio filter in the receiver chain is a bandpass filter with a 25.7 kHz bandwidth between 300 Hz and 26 kHz from AVENS Signal Equipment Corp. It is an eight order Butterworth filter designed for steep roll-off and flat response within the passband. To reject the strong leakage signal which occurs at a frequency close to DC, the filter is the first component in the audio module.

The Wind Profiler is not a true FMCW system. Time is needed for the data to be transferred from the buffer to the internal registers of the DDS requiring sweep times slightly shorter than the pulse repetition period (PRT). The abrupt steps from

sweeping to reset and sweeping again and the steep cut off of the audio filter can lead to undesirable filter ringing in the time domain. In the Wind Profiler where the audio filter is the first component in the IF section and the IF gain is 80 dB such ringing can exceed the data acquisition dymanic range of ±10 V.

To study the filter ringing, the system was terminated at the antenna input and an oscilloscope measurement was taken right after the filter. The sweep time was 8.333 ms and the PRF was 100 Hz. The filter ringing of the AVENS filter is depicted on Figure 3.10 along with the DDS trigger. The amplitude of the AVENS filter ringing exceeds 50 mV for the duration of the sweep and after 80 dB gain saturates the data acquisition. This introduced the need for a new IF filter design.

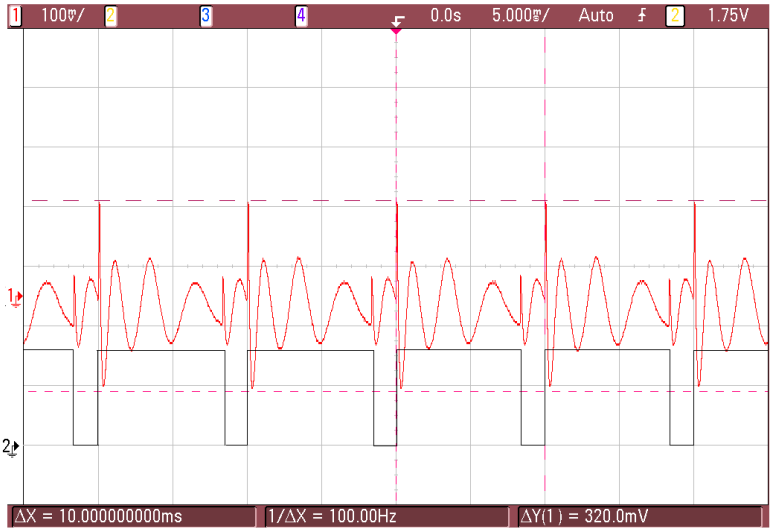

Figure 3.10. AVENS filter ringing effect

3.6.2 IF Filter Design

The major filter design considerations are (i) ensuring significant attenuation of the leakage signal, (ii) achieving trade off between filter ringing and desired minimum observable heights, and (iii) avoiding aliasing. In the worst case, the leakage cancellation should be such that the mixer is not saturated. To ensure its linear operation, the power levels at its RF port should be less than its 1 dB compression point of

9 dBm. For the IF gain of 74 dB (accounting for the mixer insertion loss of 6 dB) a leakage signal of power 9 dBm, has power of about 83 dBm at the DAQ input. The maximum power before DAQ saturation is 30 dBm. Thus, the required attenuation of the leakage beat frequency in the audio filter is about 53 dB. For better cancellation this value can be smaller.

A filter with a gentler roll-off than the AVENS filter will significantly reduce the ringing problem but it will also attenuate the low frequencies in the received spectrum corresponding to targets an near ranges. One of the primary design goals of the Wind Profiler is to be able to observe boundary layer processes at low altitudes up to few hundred meters. For a given roll-off, in order to observe phenomena closer to the radar, a decrease in the sweep time is needed (see Equation 2.6). On the other hand, this increases the leakage beat frequency which has to be attenuated by the desired amount to avoid DAQ saturation. A trade off is needed between the needed ringing reduction, leakage cancellation, and desired minimum observable heights. Table 3.4 lists the currently chosen different modes of operation and Figure 3.11 shows the beat frequency versus height for each. For a fixed, low cut-off frequency of the filter, the first mode is desirable during observation of the low boundary layer, while the second is more suitable for convective boundary layer (CBL) observations. In this case, the maximum observable height reaches more than 2 km but the information at the lower altitudes is lost.

Mode	**Sweep Time**	**PRF**	**Duty Cycle**	**Bandwidth**	**Maximum Unambiguous Velocity**	**Measured Leakage f_b**
1	6.25 ms	100 Hz	62.5%	25 MHz	±8.25 m/s	298 Hz
2	12.5 ms	60 Hz	75%	25 MHz	±4.95 m/s	149 Hz

Table 3.4. Current Wind Profiler modes of operation

To address all of the above, a high pass and a low pass filter were designed and cascaded. The high pass filter is a third order Butterworth filter with a cut-off

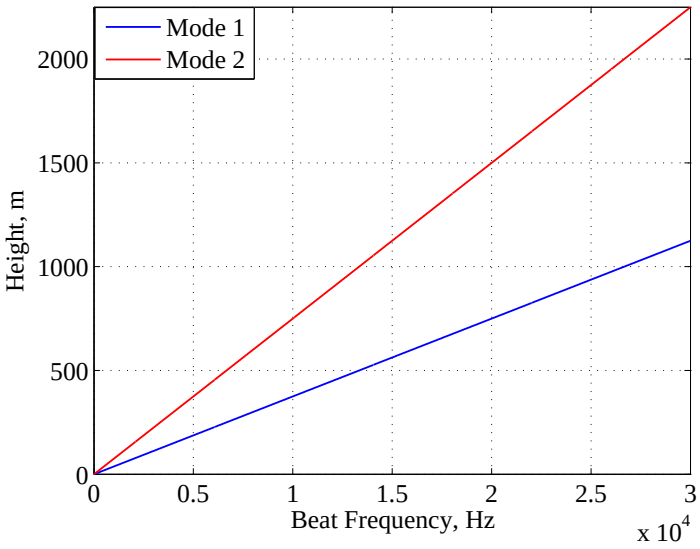

Figure 3.11. Beat frequency versus height

frequency at 5 kHz. A steeper response for the low pass filter is needed to ensure there is no aliasing. The low pass filter is a ninth order Butterworth filter with a cut-off of 26 kHz. The filter schematics, designed values and frequency response of the high and low pass filter are shown in Figure 3.12.

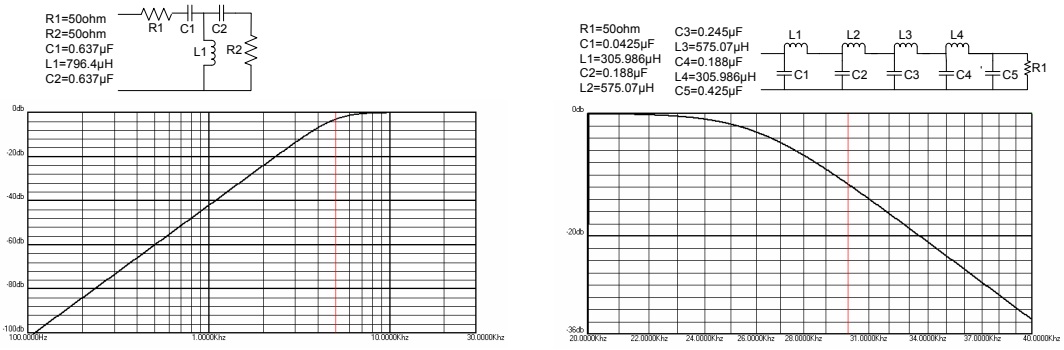

Figure 3.12. Audio filters frequency response

3.7 Expected System Performance

This section addresses the expected system performance given the current hardware configuration described in this chapter. It traces the desired signal and noise from the receiver front end to the data acquisition and discusses issues regarding available pre- and post-processing SNR, dynamic range and radar noise floor.

At the input of the Wind Profiler receiver the signal consists of atmospheric echoes, clutter and noise. The power in the returned echoes depends on the turbulence intensity which is related to the structure constant and can be found using Equation (2.15). The antenna parallax becomes negligible after 50 m of height and is not accounted for in the following calculations. Typical values of the structure constant for the convective boundary layer lie in the range between 10^{-15} to 10^{-13} $m^{\frac{-2}{3}}$. The total noise power is given by

$$P_n = kTBF = -174dBm/Hz + 10\log(25.10^6) + 3.1 = -96.9dBm, \tag{3.18}$$

where B is the RF radar bandwidth of 25 MHz and F is the radar noise figure (the noise figure measurements are discussed in Chapter 4). Figure 3.13 represents the received power from turbulence of the typical values specified above and indicates the total noise power, the minimum detectable signal and the DAQ dymanic range.

At the DAQ input the desired signal is downconverted to IF band, filtered and amplified by the total receiver gain. The received power at near ranges is affected by the frequency response of the audio filter. The total noise power at the DAQ input is

$$P_n = kTB_{af}FG, \tag{3.19}$$

where B_{af} is the audio filter bandwidth of 21 kHz, F is the total radar noise figure and G is the total receiver gain of 114 dB. The measured RF noise figure is 3.1 dB (see Chapter 4). The mixer in the receiver chain is a double side-band mixer which

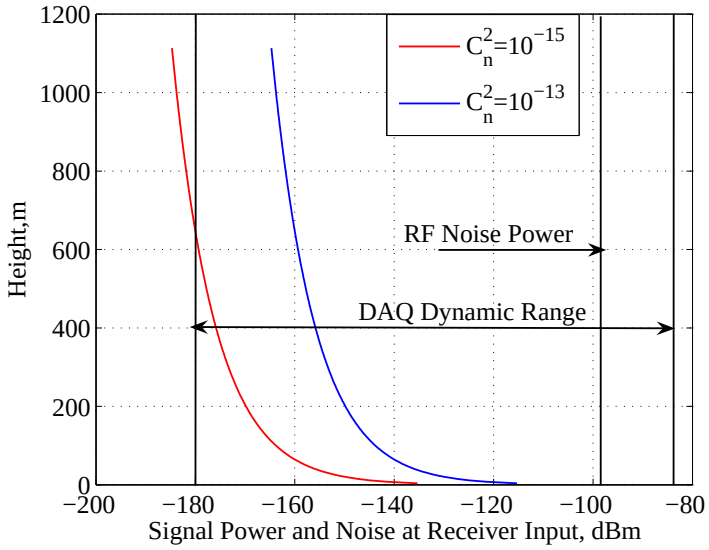

Figure 3.13. Signal power and noise at the receiver input

adds another 3 dB to the noise figure. Thus, the total noise power at the DAQ input is

$$P_n = -174dBm/Hz + 10\log(21000) + (3.1 + 3) + 114 = -10.7dBm. \qquad (3.20)$$

Figure 3.14 carries the same information as Figure 3.13 referred to the DAQ input.

As described in Section 2.3, the pulse compression or cross correlation in the Wind Profiler is done in hardware when the received echo from a particular range bin is mixed with a portion of the transmitted signal, thus confining its power within a bandwidth of $B = \frac{1}{T}$ (see Figure 2.2). When the radar is operating in Mode 1 (see Table 3.4), T is 10 ms and B is 100 Hz. The post processing scenario is depicted on Figure 3.15.

During the post processing, an FFT analysis is performed on the received data and the total noise power is spread at all frequencies up to $\frac{f_s}{2}$, where f_s is the sampling frequency. The total noise power within the 100 Hz bandwidth is

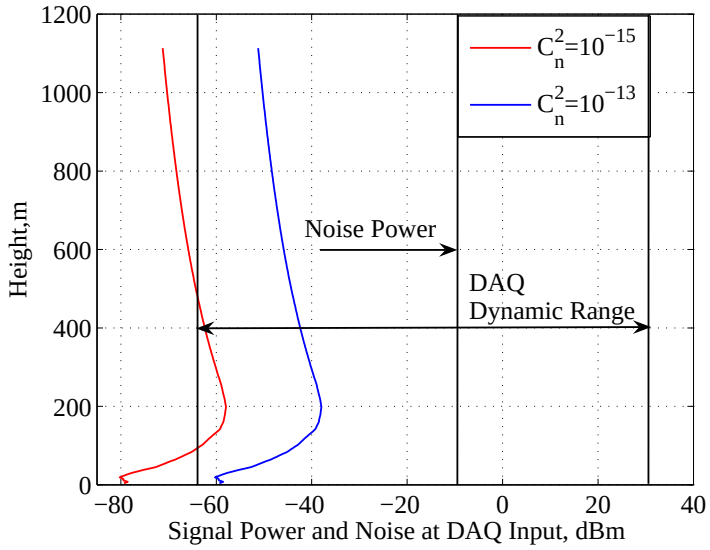

Figure 3.14. Signal power and noise at the DAQ input

$$P_n = kTBFG = -174dBm/Hz + 10\log(100) + (3.1+3) + 114 = -33.9dBm. \quad (3.21)$$

The ratio of the signal to this noise power will define the single pulse SNR of each range bin. The SNR is further increased by coherent and/or noncoherent averaging.

The pulse compression gain in the Wind Profiler is equal to 53.98 dB (see Equation 2.18) and it represents the combined effect of noise bandwidth reduction from the RF to the narrow audio bandwidth and the matched filtering, which after the FFT further "compresses" the signal to a $\frac{1}{T}$ bandwidth, where T is the pulse duration.

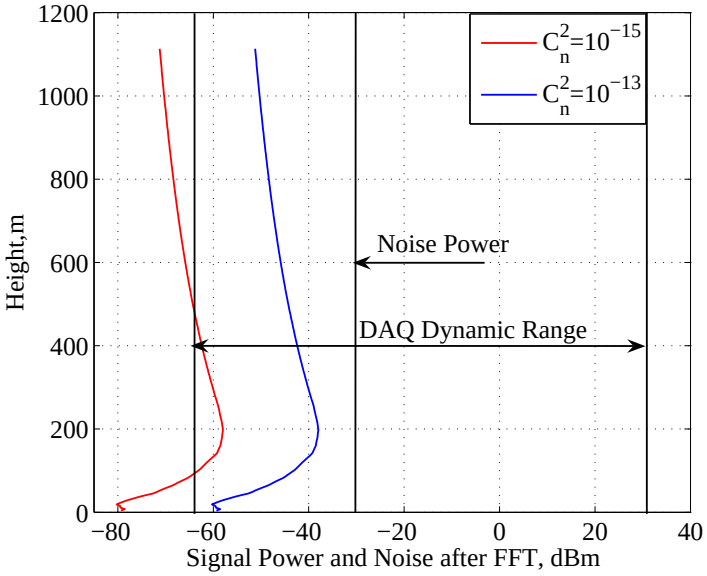

Figure 3.15. Signal power and noise after FFT

CHAPTER 4

LABORATORY HARDWARE EVALUATION

Following the changes to the hardware design of the Wind Profiler outlined in the previous chapter, a series of laboratory tests were done to evaluate the system performance. The nature of the measurements, their setup and the results are described here.

4.1 Transmit Power Measurements

The set up to measure the transmit power is depicted in Figure 4.2. The instrument used for the power measurements was the E4407B ESA-E Series Spectrum Analyzer from Agilent Technologies, with an absolute amplitude uncertainty of ± 0.5 dB. The high power RF amplifier was operated at its 1 dB point ensuring full utilization of its gain while maintaining sufficient linearity. The S21 parameters for the cables, high power coupler, and attenuators were measured separately over the chirp bandwidth and compensated in the power measurement. The expected output power is 30 W (44.78 dBm) and the results from the measurement are shown in Figure 4.1. The chirp flatness over the bandwidth was also measured and was found to be better than 0.4 dB. This result is also shown on Figure 4.1 along with the errorbars depicting the expected Spectrum Analyzer accuracy.

To ensure consistency, the transmit power was also measured with a digital oscilloscope (MSO6104A) and power meter (N1911A) from Agilent Technologies. The results from these measurements at the center frequency of 915 MHz and the expected instrument accuracies are listed in Table 4.1.

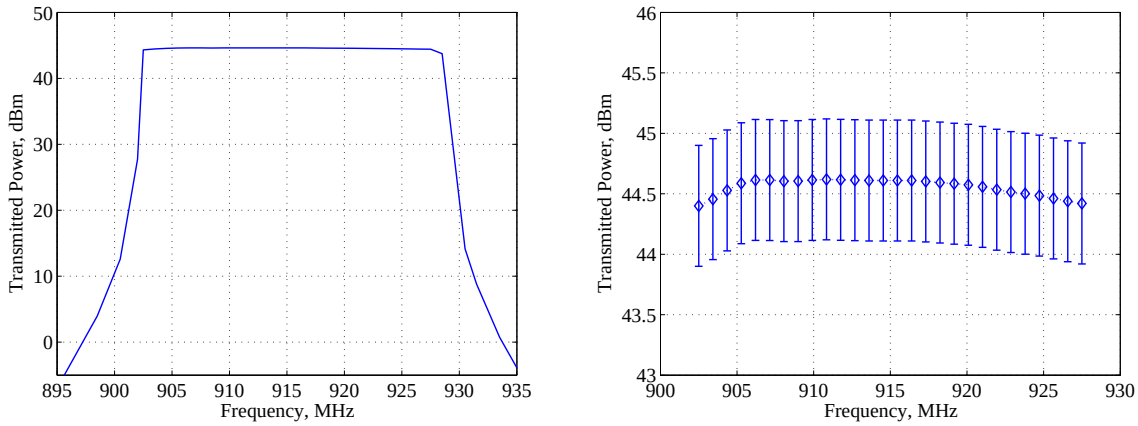

Figure 4.1. Transmit chirp power spectrum and flatness

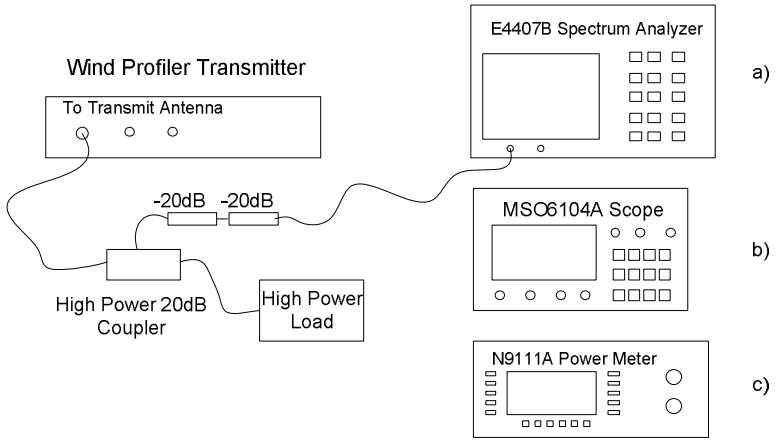

Figure 4.2. Transmit power measurements setup

4.2 Receiver Gain Measurements

4.2.1 RF Section Gain Measurements

The Wind Profiler RF section gain (up to the mixer) was measured as a function of the RF frequency across a bandwidth of 25 MHz. The E8257D PSG Analog Signal Generator with an amplitude precision better than ±0.02 dB was used to feed a monotone sinusoid with known power into the receiver, and the output was measured with the E4407B spectrum analyzer from Agilent (see Table 4.1). The frequency step

Frequency, MHz	Instrument	Accuracy, dB	Transmit Power, dBm
915	E4407B	±0.5	44.6
915	MSO6104A	±0.53	44.8
915	N1911A	±0.05	44.6

Table 4.1. Center frequency transmit power measurements

of the measurement was 1 MHz. The RF section gain for the three receive channels is plotted on Figure 4.3.

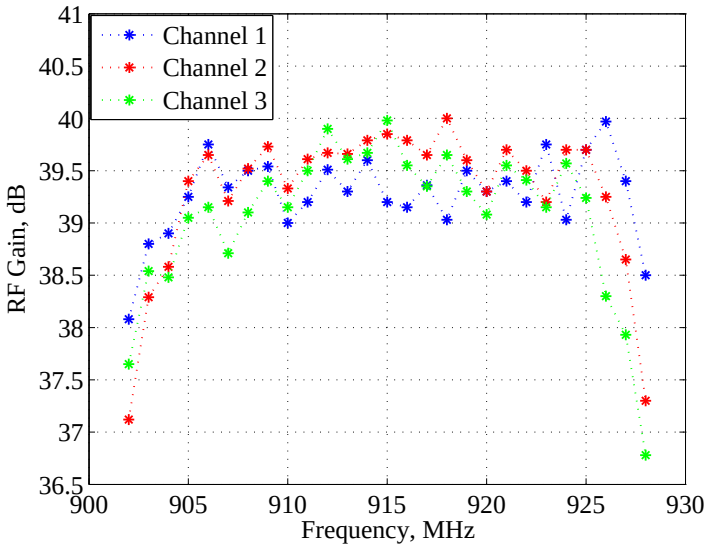

Figure 4.3. Receiver RF section gain

4.2.2 IF Section Gain Measurements

The IF section gain is dictated by the audio filter insertion loss, and the gain of the cascaded audio amplifier pair. The insertion loss of the newly designed audio filter was measured by injecting a single tone with known power level (E8257D) and measuring the output power level on the MSO6104A oscilloscope. The frequency on the E8257D was swept from DC to 60kHz. The audio filter response is depicted in Figure 4.4, along with the low frequency slope of the response. The cut off (3 dB) frequency is at the designed value of 5 KHz. The attenuation of the leakage signal

(see Table 3.4) is at least 60 dB for all modes, and the filter insertion loss within the pass band is less than 0.5 dB.

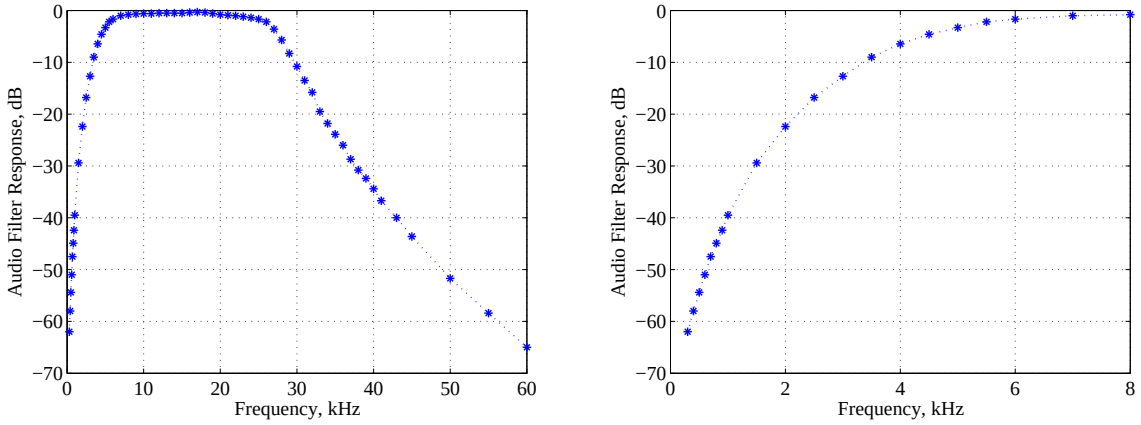

Figure 4.4. New audio filter frequency response

Ringing in the new filter was also measured with the receiver input terminated and the result is shown in Figure 4.5. It is seen that the ringing has been reduced significantly compared to the old AVENS filter. Strong ringing exists only within the first 200 μs. The amplitude of this ringing in not within the DAQ dynamic range but in this case this is not an issue because the ringing is mostly discarded by the envelope windowing in the post processing.

The gain in the IF section is provided by the two 40 dB amplifiers from AVENS Signal Equipment, Inc. These are DC-coupled voltage gain audio amplifiers with a supply voltage of ± 15 V. To avoid a DC offset at the amplifier input, a 20 μF capacitor was added in series between the filter and the amplifiers. The direct cascading of the audio amplifiers created oscillations at the output with a frequency of 500 kHz with an amplitude that saturated the data acquisition. These oscillations were created due to formation of an oscillator loop consisting of the high gain amplifier pair and the DC bias lines. The addition of $47\mu F$ bypass capacitors on all power supply lines eliminated these oscillations. The total gain of the IF section was measured over the IF bandwidth and the result is shown in Figure 4.6.

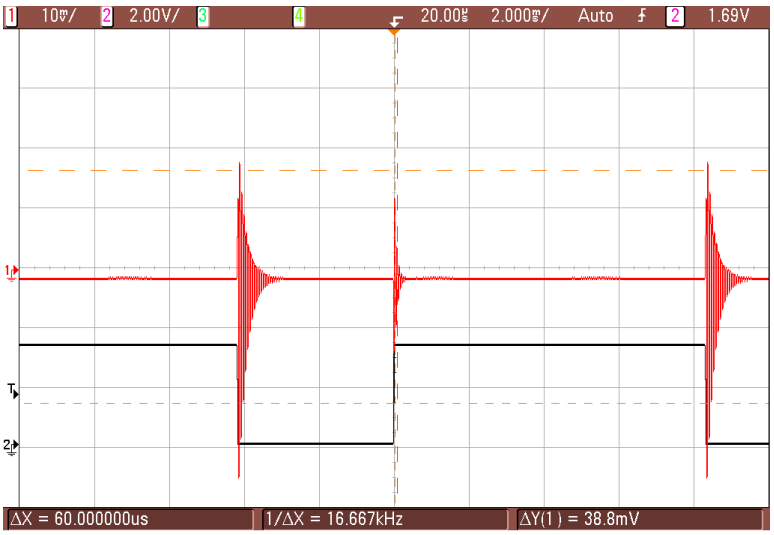

Figure 4.5. New audio filter ringing effect

Considering the gain measurements of the RF and IF section and including the conversion loss of 6 dB in the mixer, the overall gain of the Wind Profiler receiver is about 114 dB.

4.3 Noise Figure Measurements

The noise figure in a receiver is primarily determined by the first components in the receiver chain. The noise figure of the Wind Profiler RF section was measured using the Gain method, and Y-factor method.

To measure the noise figure using the gain method, the input of the device under test is terminated with a 50 Ω load, and the output power density is measured on a spectrum analyzer. The noise figure (NF) then, is given by

$$NF = P_{nd} + 174dBm/Hz - G, \tag{4.1}$$

where P_{nd} is the measured output noise power density and G is the gain of the device under test. To get a stable and accurate reading from the spectrum analyzer, the ratio of the RBW (resolution bandwidth) and VBW (video bandwidth) is recommended

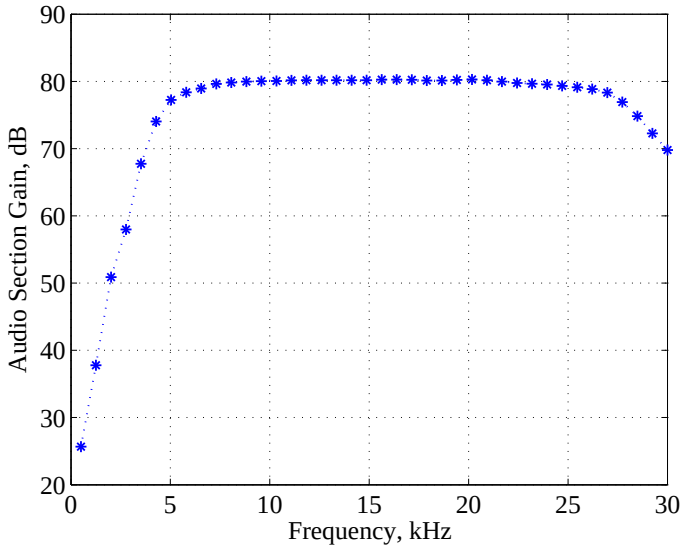

Figure 4.6. Receiver IF section gain

to be 0.3 [1]. The gain method is easy to setup and can cover a wide frequency bandwidth. It is primarily limited by the noise floor of the spectrum analyzer itself. The accuracy of the measurement is determined by the amplitude accuracy of the analyzer and by the difference between the assumed and the actual resolution bandwidth.

Measurement of the noise figure using the Y-factor method requires a calibrated noise source. These sources can output wideband noise at two different noise temperatures, T_{hot} and T_{cold} when turned on and off. They are specified by the excess noise ration (ENR) given by

$$ENR = 10log\left(\frac{T_{hot}}{T_{cold}}\right). \tag{4.2}$$

Turning the noise source on and off, the change in the output noise power density is measured with a spectrum analyzer. The noise figure can then be found using

$$NF = 10\log\left(\frac{10^{\frac{ENR}{10}}}{10^{\frac{Y}{10}}-1}\right), \tag{4.3}$$

where ENR is the standard noise figure and Y is the difference between the output noise power density when the noise source is on and off. The Y-Factor method is

more accurate for small noise figure values compared to the gain method. For the Y-factor measurement, the HP346B head was used which requires a supply voltage of 28 V. Its ENR at 1 GHz is 15.05 dB and the ENR at any other frequency can be found by extrapolating. The setup used for the two noise figure measurements is depicted on Figure 4.7.

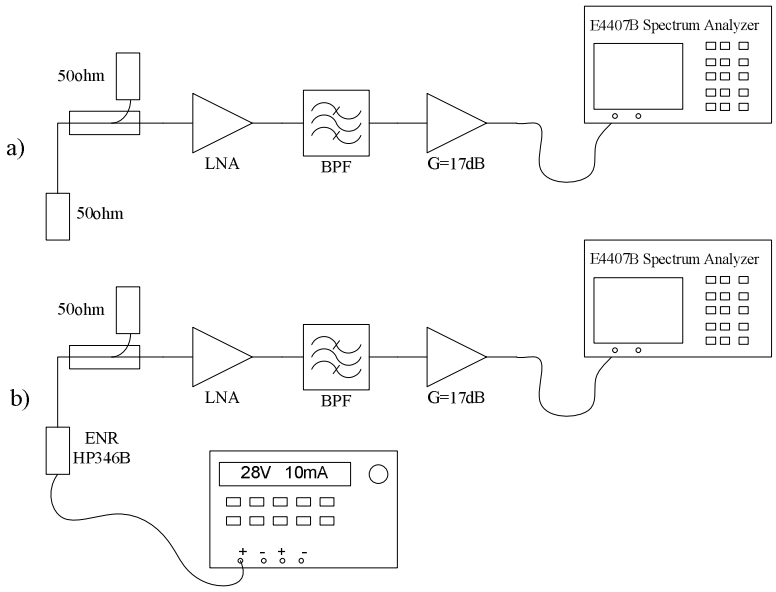

Figure 4.7. Noise figure measurement setup

The noise figure of the RF section was measured over the chirp bandwidth with 1 MHz step. At the center frequency, the measured noise figure was 1.31 dB with the gain method, 1.42 dB with the Y-factor method. These are in good agreement with the theoretically calculated value of 1.28 dB (see Section 3.5 Equation 3.16). The attenuation of the 4 m receive antenna feed line is added to the measured noise figure, to give the total noise figure of the RF section. The results, along with the confidence interval set by the expected spectrum analyzer accuracy are shown on Figure 4.8.

To verify the system noise performance, the Wind Profiler was terminated at the receiver input as well as the coupling port for the calibration and vector modulator

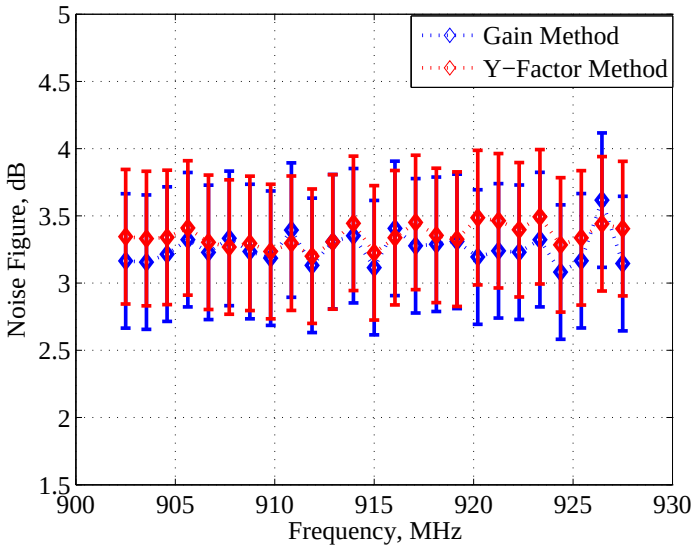

Figure 4.8. RF section noise figure

signals. Data was collected and processed in the following manner: (i) the time series was read from the specified channel, (ii) a Hanning window was applied to the time series of each profile, (iii) 100 profiles were stored in a matrix, FFT performed and the mean removed, (iv) the matrix was multiplied by its conjugate and the average of the power plotted. Figure 4.9 shows the power spectrum of the averaged profiles. It is seen that the noise floor is at -25.6 dBm per 100Hz of resolution bandwidth instead of the expected value of -33.9 dBm (see Section 3.7). After a series of tests, the source of that excess noise was found to originate in the AVENS audio amplifiers. The internal noise of the amplifiers referred to their input is specified to be 50 μV RMS for the bandwidth of DC to 100 kHz. This sets the device noise floor at -123dBm/Hz. The total gain of the audio amplifiers is 80 dB giving a noise power density at the DAQ input of -43dBm/Hz. For the resolution bandwidth of 100 Hz that is a noise power density of -23 dBm. The 2.4 dB difference between that value and the value from the measurement is due to the windowing that is performed on the data before the FFT.

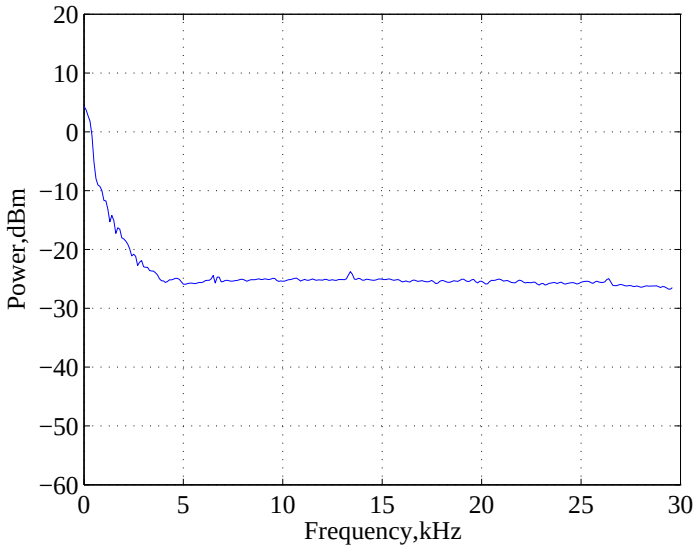

Figure 4.9. Wind Profiler received noise power spectral density

The high gain in the IF section requires a procurement of a new ultra low noise audio amplifiers. An alternative to that would be to increase the gain of the RF section, thereby increasing the signal level to the audio amplifier input and reducing the IF section gain. However, the RF gain is limited by transmitter leakage concerns.

4.4 Delay Line Measurements

A 2 μs acoustic delay line was integrated in the Wind Profiler hardware to form an internal calibration loop for system monitoring. The calibration loop is described in Section 3.3 and the delay line specification are given in Table 3.3. The amplitude modulated delayed chirp from the calibration loop produces a sinusoidal signal of frequency f_b corresponding to the delay in the delay line, and another sinusoidal signal corresponding to the first sideband of the amplitude modulation at the mixer IF port.

The transmitted chirp is coupled into a splitter through the 20 dB coupler in the transmitter chain. The splitter splits the signal to the vector modulator and the

calibration loop. A cascade of 30 and 10 dB attenuators attenuates the calibration loop signal before feeding it into the delay line input. The nominal insertion loss of the delay line is 11.5 dB. The triple travel signal of the delay line amplitude modulates the chirp. Figure 4.10 shows the input chirp to the delay line and its amplitude modulated output in the time domain.

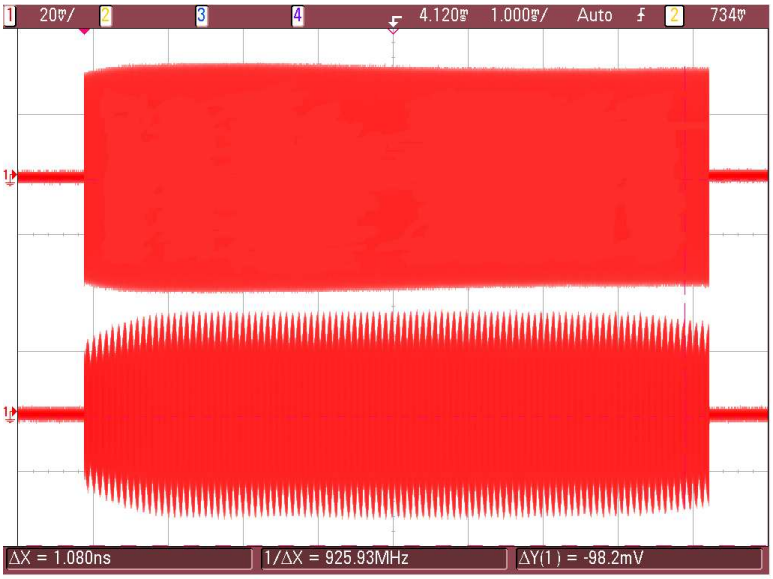

Figure 4.10. Effect of the triple travel signal in the delay line

After the delay line the signal is attenuated another 50 dB, split into three for the three receiving channels and coupled to the receiver chain through the 20 dB coupler along with the canceling signal from the vector modulator. The measured total attenuation on the calibration loop path is 150.6 dB which is in very good agreement with the expected value of 149.3 dB. The beat frequency after the mixer in the first mode of operation is 8 kHz. Using the knowledge of what the transmitted power and the total attenuation of the calibration loop is, the power in the received signal with frequency f_b=8 kHz was calculated to be about 8 dBm.

The frequency of the signal modulating the delayed chirp is (see Equation 3.2) 16 kHz and the triple travel chirp was expected at three times the dominant frequency f_b. To test the calibration loop, the system was terminated at the receiver input and

at the vector modulator output, and the delay line signal was coupled into the receiver chain. Data was collected and processed in the same way as in the case of the noise floor measurements (see Section 4.3) but with no mean removal so that the delay line signal is seen. The result is shown on Figure 4.11 where the dominant 8 kHz frequency is seen along with the triple travel chirp at 24 kHz which is about 16 dB below the main 8 kHz signal, as expected.

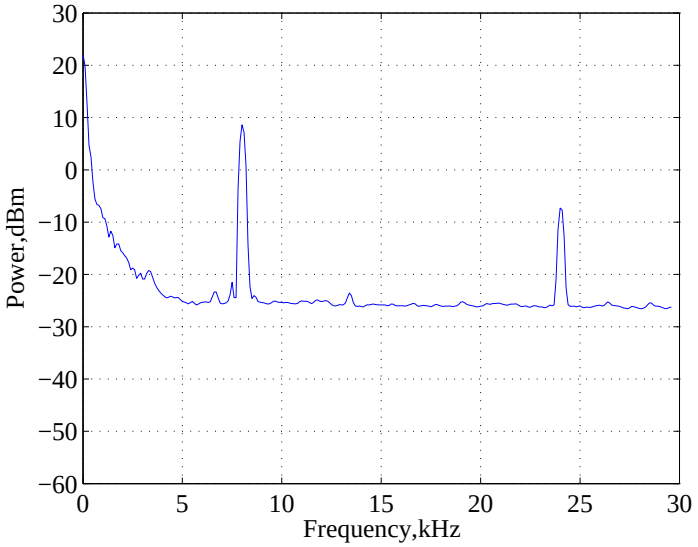

Figure 4.11. Received power spectral density from the delay line

Experimentally validating the expected performance of the delay line, it was used to determine the true available SNR and mininum detectable signal in the Wind Profiler. For the given attenuation on the delay line loop using Equation 3.4 the volume reflectivity of the equivalent target was calculated to be 6.02x10$^{-10}m^{-}$1. That reflectivity is related to the structure constant by the relationship in Equation 2.4 to give a structure constant of $C_n^2 = 1.1\text{x}10^{-9}$. Using that, Figure 4.12 depicts the minimum detectable structure constant given the current Wind Profiler configuration for a single pulse post-processing SNR of 0 dB. It is seen that the radar can detect only very high values of the structure constant which correspond to high intensity refractive index fluctuations due to very strong turbulence. Hence, averaging in required to

improve the SNR and allow for smaller structure constant values to be detected, reducing the temporal resolution of the Wind Profiler.

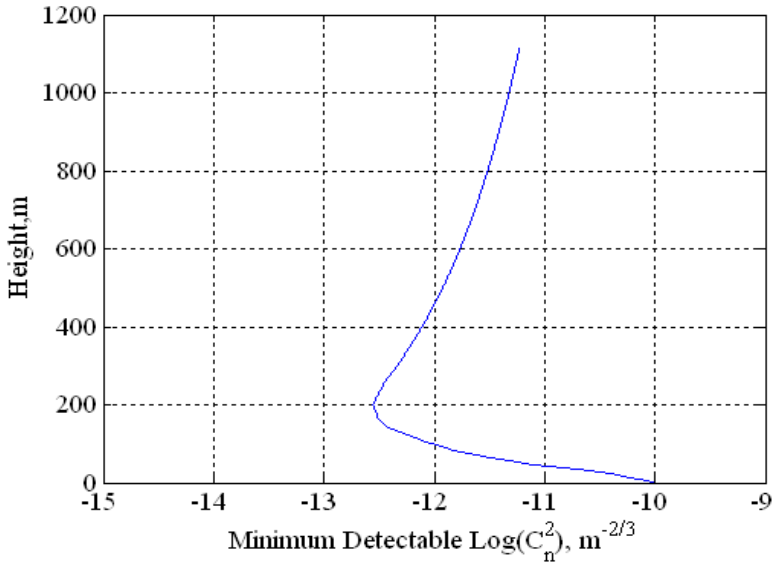

Figure 4.12. Minimum detectable $\log C_n^2$ before averaging

4.5 Vector Modulator Measurements

The available isolation between the transmit and receive antennas in the Wind Profiler is not sufficient to ensure linear operation of the mixer in the receiver chain. To solve this, an active cancellation loop consisting of a vector modulator was integrated into the radar system. The vector modulator and its hardware implementation are described in Section 3.4. The isolation between the antennas determines what the minumum required cancellation that ensures linear operation of the mixer is. In the current configuration, two antennas are mounted on the MIRSL FMCW truck, with a separation distance of 2.75 m, and the measured isolation between them is about 71 dB. Safe mixer input power levels are about 8 dBm and the RF gain prior to the mixer is 40 dB. That sets the minimum required cancellation to about 6 dB. The laboratory set up used for the cancellation loop testing is depicted in Figure 4.13.

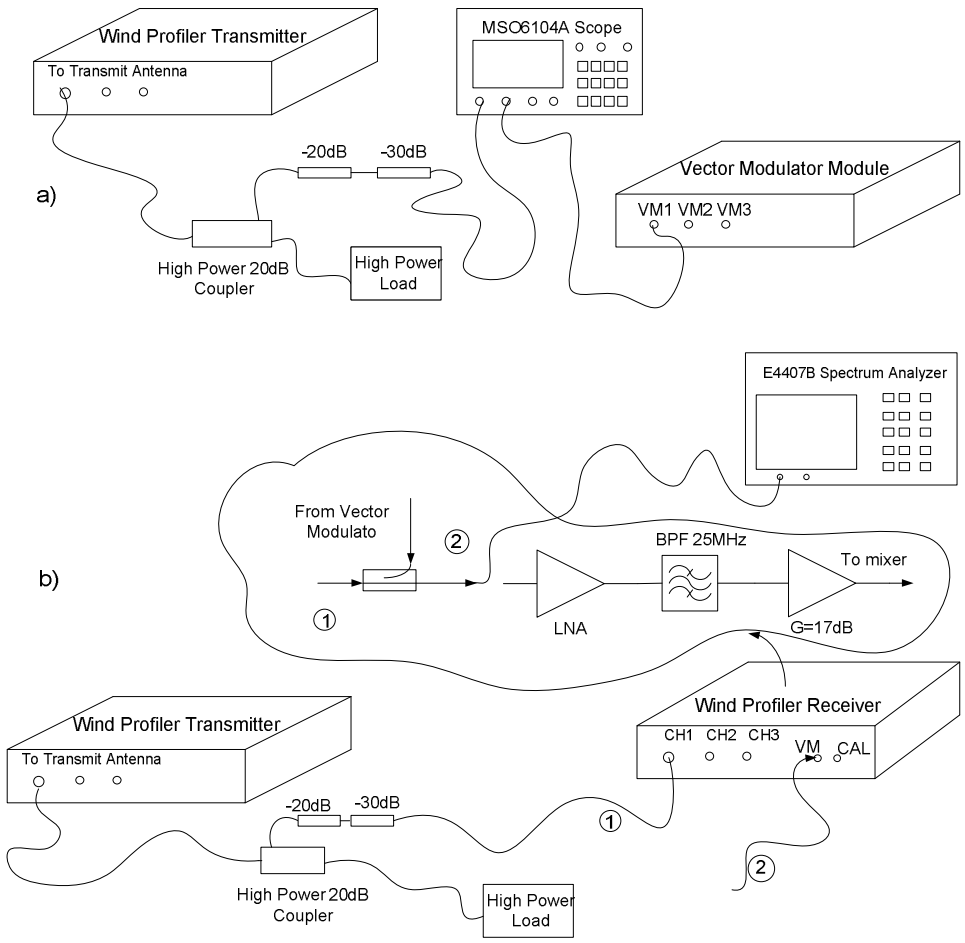

Figure 4.13. Setup used for cancellation loop tests

Cancellation measurements in the lab were carried out by mimicking the transmitter leakage using a 20 dB high power coupler and appropriate attenuation as shown on Figure 4.13. The first step in the cancellation process is to align the leakage signal and the canceling signal from the vector modulator in time. The transmitter leakage thus generated was fed into one of the digital oscilloscope (MSO6104A) channels. The canceling signal from the vector modulator output was fed into another oscilloscope channel. The total round-trip length of the antenna feed lines is about 12 m and the leakage always lags the canceling signal. Additional cable was added in the canceling signal path to visually align it on the oscilloscope with the leakage signal in time.

After aligning the two signals in time, the leakage signal was fed into the receiver input and the canceling signal is coupled to the receiver chain through the 20 dB coupler. The output of the coupler was connected to the spectrum analyzer. The user program controlling the analog output (PD2-AO-16/16) card that generates the I and Q control signals was started with some initial gain and phase value. By observing the cancelled signal on the spectrum analyzer, the gain-phase parameter space is manually searched for an appropriate setpoint. As mentioned in Section 3.4, the achieved cancellation is limited by the amplitude error between the leakage and the canceling signal at each of the chirp frequencies. The smaller the signal to be cancelled is, the less the amplitude error can be tolerated for a given cancellation. Figure 4.14 shows the gain error in the vector modulator for different phase setpoint.

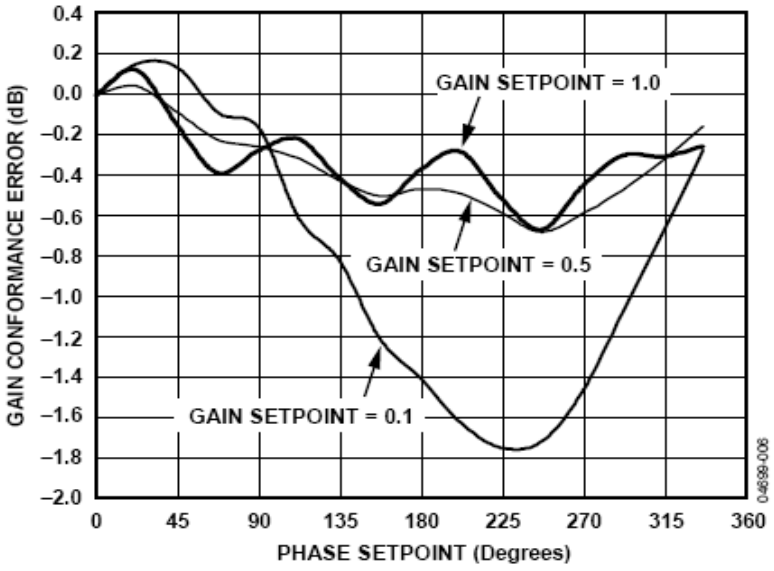

Figure 4.14. Vector modulator gain error

Figure 4.15 shows the leakage before and after cancellation. The maximum achieved cancellation during the laboratory tests was about 15 dB which is sufficient to ensure linear operation of the RF mixer. For better cancellation the amplitude error between the leakage and the canceling signal should be less than 0.7 dB.

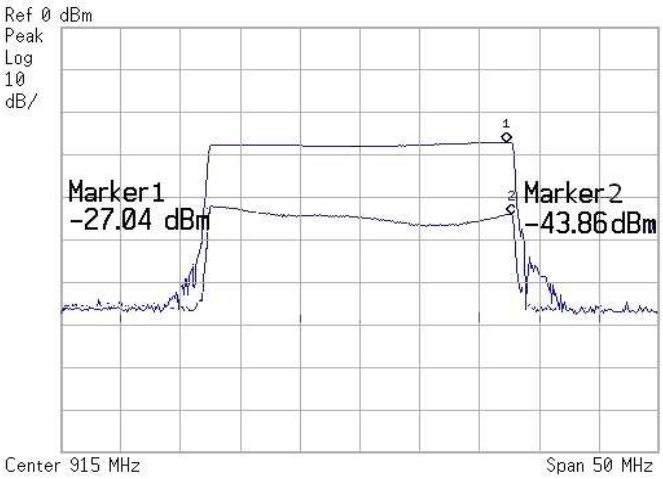

Figure 4.15. Achieved leakage cancellation in the laboratory

To test the whole system performance with the canceling loop included into the radar system, the cancelled leakage was fed into the receiver chain (see Figure 4.13) and data was collected. With the leakage signal being sufficiently cancelled, the system performance was expected to be the same as in the case where the receiver is terminated. The data was processed in the same way described in Section 4.3 and the result is plotted on Figure 4.16.

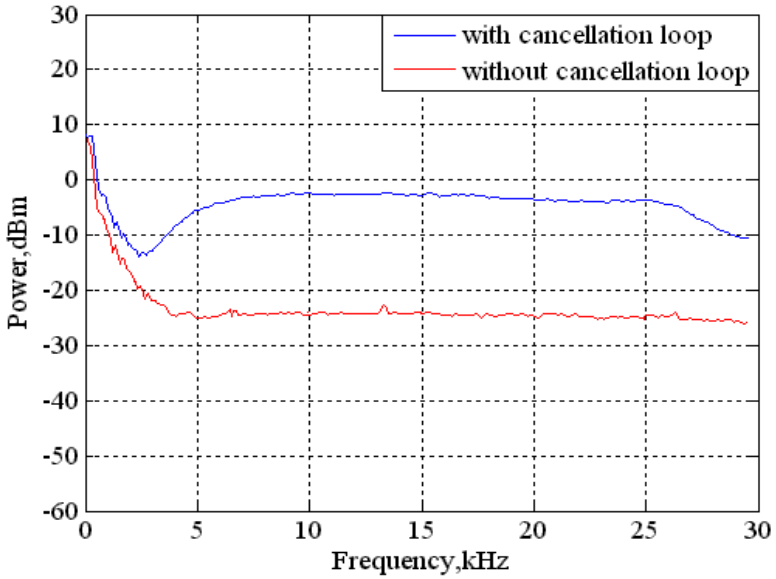

Figure 4.16. Received noise power spectral density with the cancellation loop

It is seen from Figure 4.16, that the noise floor has increased by about 22 dB compared to its value in Figure 4.9. This increase in the noise floor deteriorates the radar SNR to unacceptable values. The additional noise was found to originate in the analog output (PD-2-AO-16/16) card generating the vector modulator control signals. The amplitude range of the analog output card is fixed to ±10 V and the specified RMS noise voltage is to occupy the two LSBs for the frequency range of DC to 10 kHz. This sets the card output noise floor to -91 dBm/Hz. This noise rides on the control signal making the canceling signal noisy. The noise thus introduced into the receiver chain, renders the receiver input noise to a value significantly higher than the expected value of -174 dBm/Hz.

The voltage on the control lines vary between 250 mV and 750 mV. To reduce the noise coupled into the canceling signal, that voltage can be increased to fill the card dynamic range and the control line voltage can be provided by a voltage divider. Such a setup will effectively reduce the noise power coupled into the vector modulator while maintaining the same peak-to-peak setting on the control lines. This solution was put to test by adding a simple voltage divider consisting of two resistors in series with values of 1 kΩ and 120 Ω between the analog output card and the input to the vector modulator control signals. The expected reduction in the noise is $20\log(0.107)$ or 19.4 dB. The results of the test are shown on Figure 4.17.

The maximum control signal voltage is 750 mV while the maximum analog output card voltage is 10 V. Adjusting the values of the voltage divider such that the control signal range fills up the maximum range of the analog output card, the noise coupled to the vector modulator signal can be reduced by as much as 21.8 dB. That can bring the Wind Profiler noise floor to its current value but will still keep it 8 dB above the ideal system noise floor.

In its current configuration, the bandwidth of the control signals is 230 MHz. The vector modulator evaluation board allows for reduction of that bandwidth by

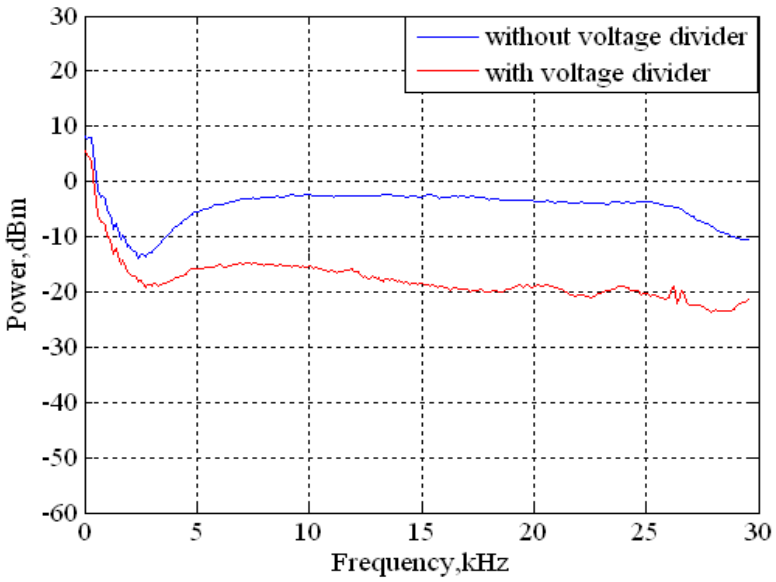

Figure 4.17. Reduction of noise coupled through the vector modulator

installing external capacitors on the control lines on the board. In the case of the Wind Profiler, the control signals for the vector modulator are DC signals which allows for additional reduction of the coupled noise if both, the voltage divider and external capacitors are integrated into the board circuit.

The requirement for a new design of an ultra low noise audio amplifier presents the possibility for redistribution of the gain in the receiver. Part of the receiver gain in the RF section can be moved down to the IF section. This can eliminate the need of a vector modulator loop for transmitter leakage cancellation. In case of a future deployment scenario where active cancelling of the transmitter leakage is needed, the proposed solution for noise coupling reduction should be implemented.

CHAPTER 5

FIELD DEPLOYMENT

During the laboratory tests the system performance was well understood. The error sources that deviate the real performance from its ideal characteristics were identified, and plausible improvements in the system architecture were analyzed. To verify the radar behavior in field deployment conditions, and identify possible additional error sources, a series of test deployments were conducted during the months of May and June 2009. The radar hardware was mounted on an instrument rack and placed inside the cabin of the S-band FMCW truck. The S-band antennas were removed and two of the Wind Profiler antennas were mounted on the existing rack on the truck bed. The S-band truck is equipped with a generator that provides power for the radar and the equipment, making the Wind Profiler independent and mobile. During the deployments presented here the radar was operating in the first mode (see Table 3.4). The results from the first few deployments are discussed in the following chapter. They will bring important insight before the implementation of SA technology in the Wind Profiler hardware is carried on.

5.1 Deployment at the horse farm

The atmospheric refractive index fluctuations represent a very weak target, orders of magnitude smaller than the ground clutter. It is important that the Wind Profiler is deployed in as clutter free environment as possible. The UMASS horse farm located west of the campus between Rt. 116 and N Maple St. is one of the few open areas around Amherst, which made it a good candidate for the first field deployment.

The radar was deployed at the southeast corner of the horse ring on May 6th 2009. The day was partly cloudy with humidity between 60-70%. The isolation between the antennas was measured first. Then, an active cancellation of the leakage was attempted as described in Section 4.5. The leakage power and the best achieved cancellation are shown on Figure 5.1.

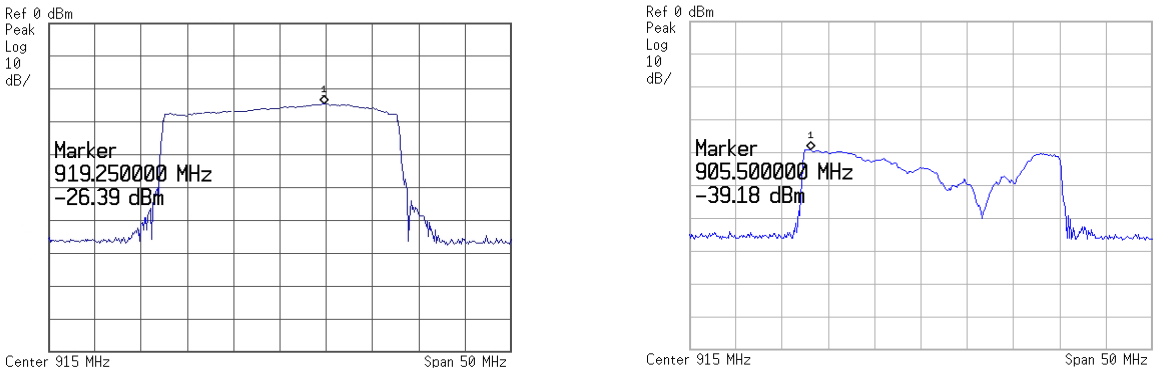

Figure 5.1. Transmitter leakage and achieved cancellation

The transmitter leakage could not be cancelled better than 13 dB. The reduction in the achieved cancellation, compared to the laboratory tests measurements was probably due to near range clutter that becomes superimposed on the transmitter leakage through the antenna backlobe and sidelobes. The achieved cancellation was sufficient for linear mixer operation and before data collection was initiated the received signal was measured at the audio amplifiers output to test for possible saturation of the DAQ. The received signal was clutter contaminated and well exceeded the available DAQ dynamic range. To fit the received signal into that range a 10 dB attenuator was added before the mixer. This reduced the expected radar SNR by 10 dB as the radar noise floor is fixed at a value set by the cascaded audio amplifier pair (see Section 4.3). The minimum detectable C_n^2 in that case is plotted in Figure 5.2. Data was collected under these conditions. Thirty minute long files were stored on the radar hard drive and processed in two steps.

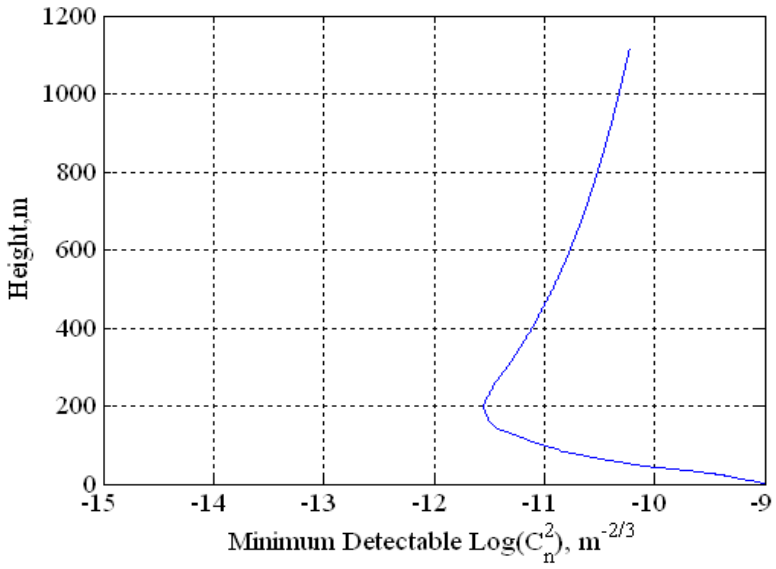

Figure 5.2. Minimum detectable signal before averaging during deployment

The raw binary file was first processed with the IDL procedure called windprof_process. The steps in the processing are depicted in Figure 5.3. By removing the mean from the FFT ground clutter rejection and rejection of stationary targets is achieved. The pulse-pair technique described in Section 2.3 is used to estimate the mean Doppler velocity. After the processing of the raw binary file, the estimated products of interest are stored in a file with the same name and extension "img". Another IDL procedure called windprof_display reads the ".img" file and after range correction created 2D images of the radar reflectivity and Doppler velocity.

Figure 5.4 represents data collected from 17:38:00 to 18:08:00 EST time. The noncoherent integration time was one second. The received signal is entirely clutter dominated and no discernible boundary layer features were observed in the reflectivity image. A periodic target movement in the range between 50 m to 350 m was observed. The features of that target suggested that it has entered the received signal through the antenna sidelobes. It was later identified as a horse rider that was going in circles around the horse ring during the experiment (see Figure 5.5). The bright line at 750 m was an artifact in the radar.

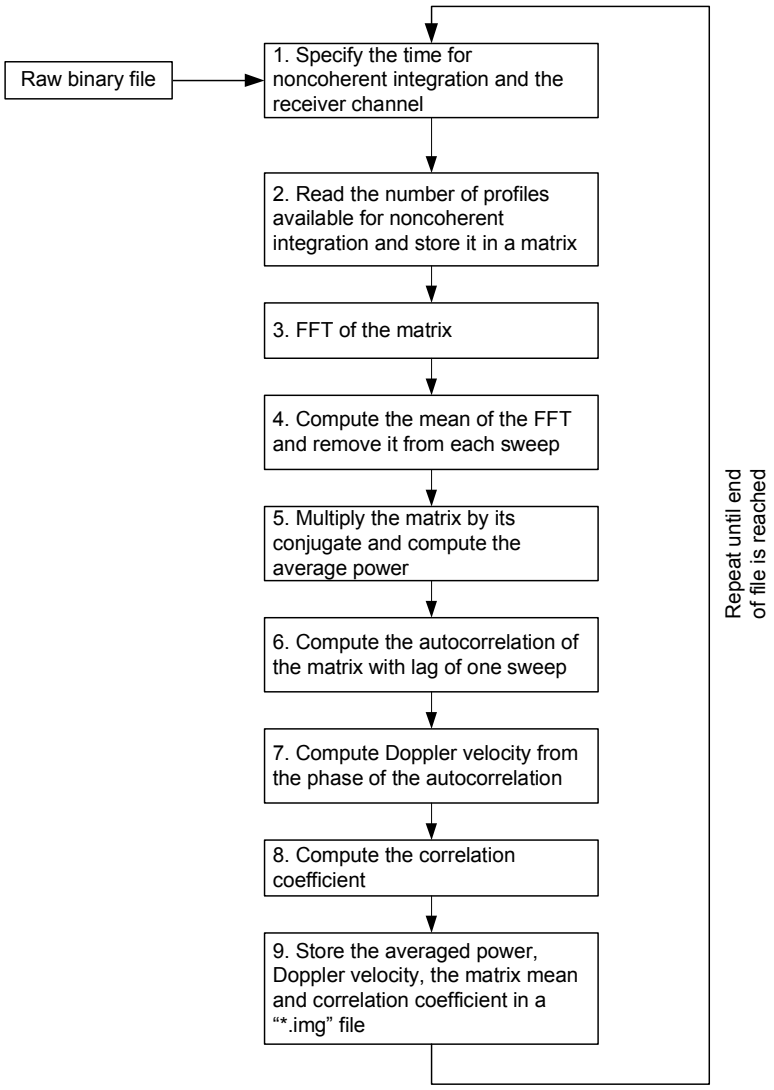

Figure 5.3. Raw binary file processing chain

The Wind Profiler antennas are commercial communication antennas that were purchased from Gabriel Antennas. The back to front ratio for the antennas is specified to be -22 dB but no antenna pattern was provided. That first deployment results suggested that the antenna sidelobe and/or backlobe levels are not sufficient given the dominant clutter in the received data. The antennas mounted on the FMCW truck bed are elevated from the ground about 3 m. It was suspected that the clutter primarily entered the receiver through the backlobe illuminating the ground.

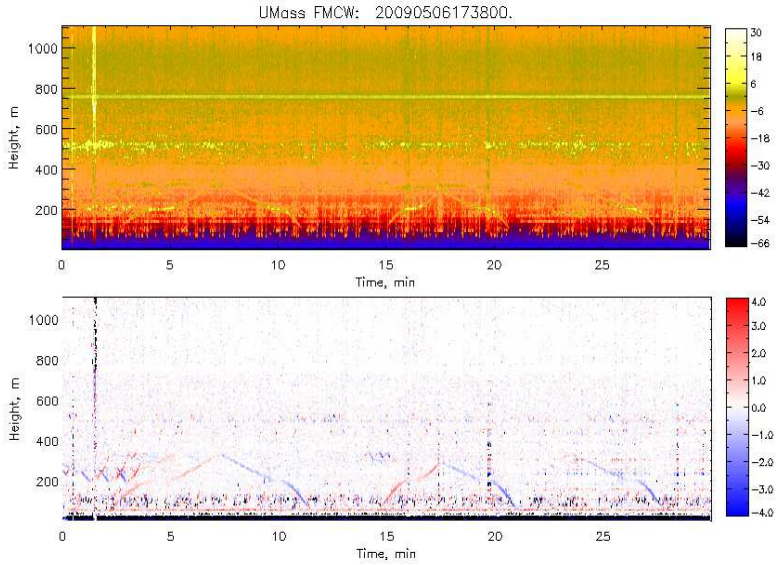

Figure 5.4. Returned power and Doppler velocity during deployment - May 6th 2009, 17:38:00 local time

In search of a better location, the radar was deployed on the side of Cemetery Rd in Hadley, MA on May 8th 2009. The site consisted primarily of plowed fields with almost no buildings in the vicinity. The deployment procedure and data processing followed the same steps as described here. In this case again, the clutter was the dominant signal in the receiver forcing 10 dB attenuation to be added to the receiver chain. Figure 5.6 shows another 30 minutes of data collected during the deployment. A target moving away and towards the radar periodically was clearly seen on the Doppler image. This was suspected to be a tractor plowing the nearby field. This was later verified when the range to the tractor was superimposed on an image from Google Earth (see Figure 5.7).

5.2 Deployment at Tilson Farm

The Cemetery Rd. site is the most suitable in the area in terms of minimizing the clutter. Before taking the truck far in search of a better deployment location it was decided that building a shroud fence around the antennas is a fast and inexpensive

Figure 5.5. Deployment location at the UMASS horse farm (image produced by Google Earth)

way to improve the antenna backlobe/sidelobe levels. The truck was taken to Tilson farm (UMASS deployment site off of Tilson Farm Rd, Amherst, MA) and two of the four available antennas were assembled and leveled on the ground. A shroud fence was build around them using hardware cloth. The fence started at the ground level and reached 15 to 20 cm above the antennas. The two antennas with the shroud fence around are depicted on Figure 5.8. The FMCW truck was parked next to the antennas.

Under these condition the Wind Profiler performance was tested again. The antenna isolation improved by 2 dB but the improvement in clutter rejection was insignificant. That suggested that the main path for the clutter is not the backlobe but the antenna sidelobes.

At this point, before undertaking the task of building a higher fence or looking for a suitable deployment site, it was decided to test the radar sensitivity using rain as a target with known reflectivity. The received power from a volume filled with rain

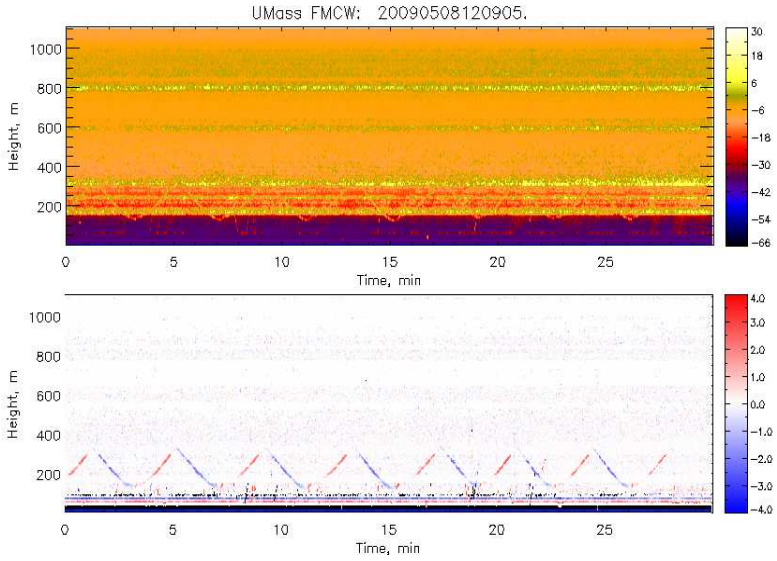

Figure 5.6. Returned power and Doppler velocity during deployment - May 8th 2009, 12:09:05 local time

drop scatterers and antennas with Gaussian shaped beams is given by [10]

$$P_r = \frac{P_t G^2 \Theta^2 \Delta R \pi^3 k^2 Z 10^{18}}{512(4ln2)R^2\lambda^2}, \tag{5.1}$$

where $k^2 = 0.93$ for centimiter wavelengths, and Z is the radar reflectivity factor in units of $\frac{mm^6}{m^3}$. Comparing this with Equation 2.15 and using Equation 2.4, a relationship between Z and C_n^2 is derived as

$$C_n^2 = \frac{\pi^5 k^2 Z 10^{18}}{1.52\lambda^{\frac{11}{3}}}. \tag{5.2}$$

In the morning of June 9th 2009 data was collected from 9:01:10 to 9:31:10 EST time during a rainfall. The average reflectivity between 9:02:10 and 9:03:10 was estimated between 800 to 1000 m height above ground level. This region was chosen for two reasons - (i) it can be assumed that it is clutter free, (ii) the computed rain rate was later compared with the data from the NexRAD KBOX radar located in Boston, MA. KBOX has an elevation angle of 0.5 deg and its radar beam passes above

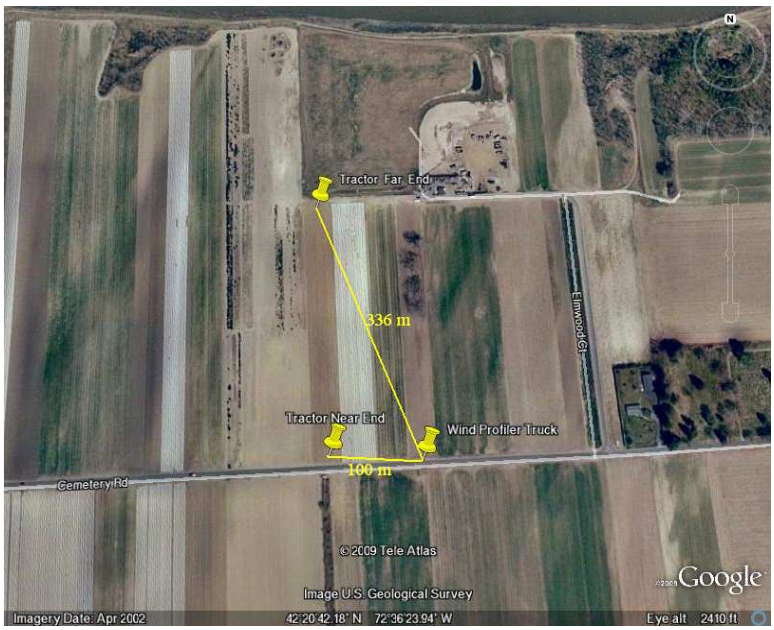

Figure 5.7. Deployment location at Cemetery Rd, Hadley, MA (image produced by Google Earth)

Amherst at a height of about 1.1 km. Using Equation 5.2, the equivalent C_n^2 values were computed and the results are shown on Figure 5.9.

To verify the estimated values for the reflectivity factor, dataset for the KBOX base reflectivity from the NexRAD archives (http://www.ncdc.noaa.gov/nexradinv/) was downloaded for the same time period. Figure 5.10 depicts the base reflectivity seen by KBOX between 9:00:00 and 9:05:00 EST time. The exact location of the Wind Profiler truck is indicated on the image. It can be seen that the estimated reflectivity factor from the Wind Profiler coincides well with the KBOX data. This experiment verified that the Wind Profiler antennas were well aligned in terms of look direction and polarization.

Given the reflectivity factor, the equivalent C_n^2 values, computed using Equation 5.2, lie around $2\text{x}10^{-11}$. Comparing this with the calculated minimum detectable C_n^2 (see Figure 5.2), it is seen that such C_n^2 values won't be detected unless averaging is performed. Indeed, that was the case as seen on Figure 5.11. Noncoherent averaging

Figure 5.8. Shroud fence built around the Wind Profiler antennas

of one second was performed. That increased the SNR by 10 dB and the rain was easily identified on Figure 5.12. Towards the end of the data file the rain diminished and fell below the radar noise floor. The KBOX base reflectivity data indicated a reflectivity factor of 20 dBz at that time.

The measured mean Doppler velocity of rain was about -6.5 m/s. The terminal fall velocity of droplets is dependent on their diameter and a relationship between the two was developed by Gunn and Kinzer in 1949 [13]. Burrows and Attwood studied the drop size distribution for a given rain rate [4]. Finally, we used the Marshall-Palmer relationship between the reflectivity factor Z (mm^6m^{-3}) and the rain rate R (mm/h), given as $Z = 200R^{1.6}$, to find what the mean drop size was (using the results of Burrows and Attwood). For the reflectivity factor measured by the Wind Profiler (see Figure 5.9), the rain rate R lay between 5 and 7 mm/h [9]. More than 50% of the drops contained within the volume of interest have a diameter between 1.5 mm and 2.5 mm [4]. The mean terminal velocity of drops with such diameter, using the results of Gunn and Kinzer, is about 6.2 m/s, which was in very good agreement with the Wind Profiler estimates.

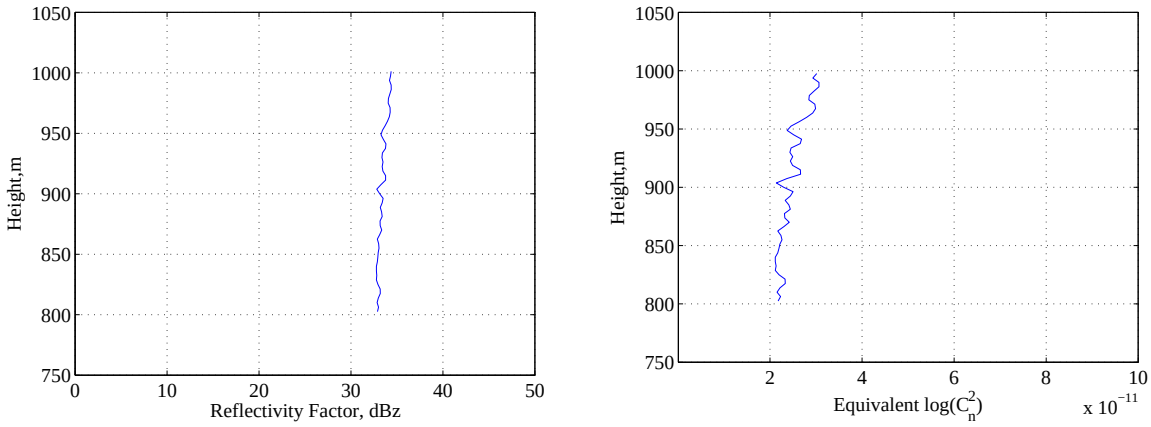

Figure 5.9. Computed reflectivity factor and the equivalent C_n^2

Numerous models for the drop size distribution and relationships between the reflectivity factor Z and the rain rate R under different atmospheric conditions have been developed and extensively studied, but they are out of the scope of this thesis. The purpose here was to qualitatively analyze the Wind Profiler measurements of Doppler velocity.

The field deployment results described in this chapter confirmed the expected radar performance after the laboratory tests and proved very helpful in identifying the current major error sources. The lessons learned helped in generating useful recommendations for future work.

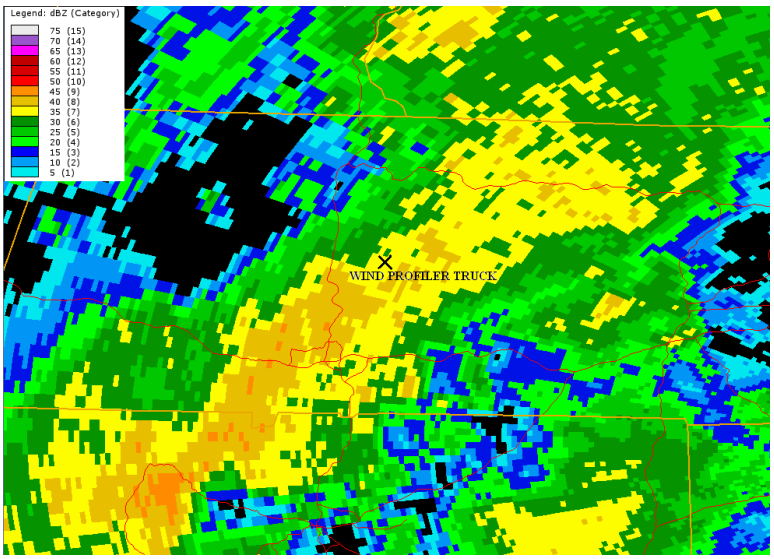

Figure 5.10. KBOX base reflectivity between 9:00:00 and 9:05:00 EST time on June 9th 2009 (courtesy of National Weather Service)

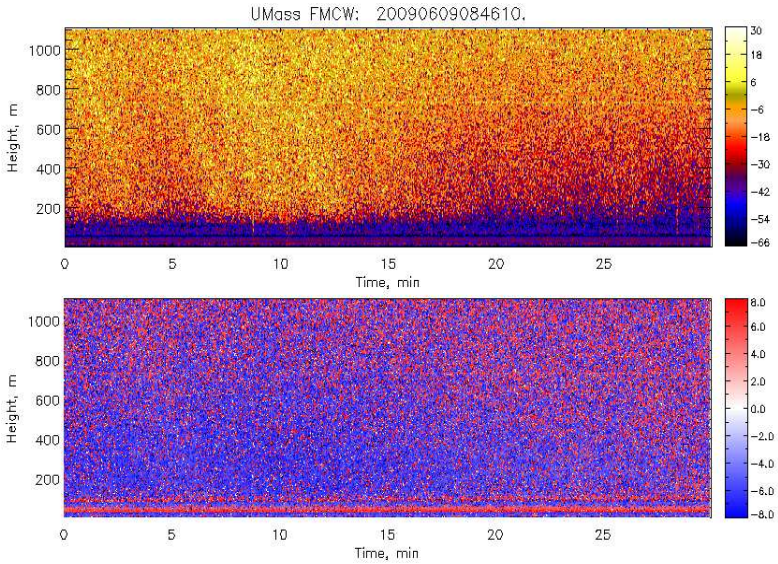

Figure 5.11. Wind Profiler reflectivity and Doppler velocity - June 9th 2009 starting at 9:01:10 local time (no averaging)

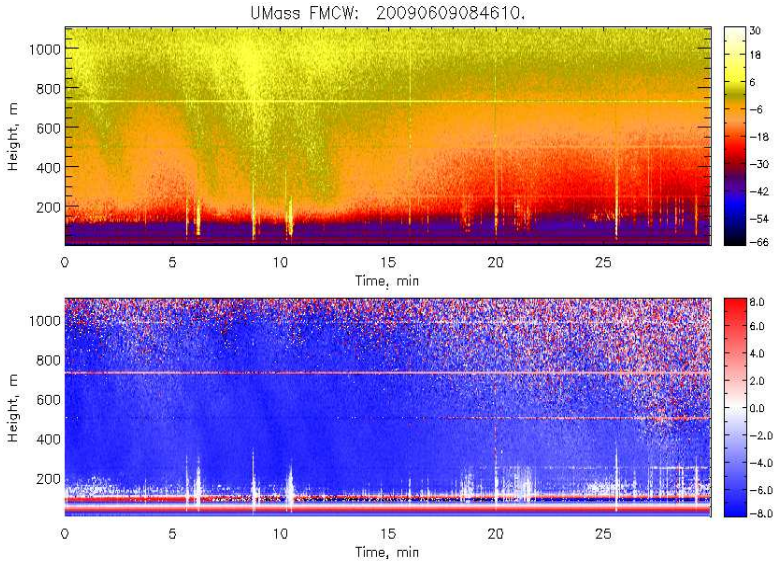

Figure 5.12. Wind Profiler reflectivity and Doppler velocity - June 9th 2009 starting at 9:01:10 local time (1 sec averaging)

CHAPTER 6

CONCLUSIONS AND FUTURE WORK

The work presented in this thesis is a detailed description of the research efforts to develop an UHF FM-CW Wind Profiler for boundary layer studies that will eventually utilize spaced antenna technique for retrieving horizontal wind velocities, thus providing information about 3D wind fields. The Wind Profiler design and development was initiated in the summer of 2006 by Prof. Frasier and research engineer PeiSang Tsai. The FPGA and DDS system were later integrated by visiting Master's student Albert Genis. This chapter contains a summary of the research work conducted from then on to the Wind Profiler present stage. Valuable conclusions and recommendations for future work are included as reference for further refinement in the development and deployment of the Wind Profiler.

6.1 Summary of Work

The main body of the thesis includes the radar hardware upgrade, hardware evaluation and laboratory tests, and first field deployment results.

The hardware upgrade consisted of the following.

(i) The ground coupled noise in the receiver chain was eliminated. The noise entered the receiver through the common ground between the solid state RF amplifier and some receiver components. The amplifier is now housed in a separate radar box and powered independently by a separate power supply.

(ii) The spurious signals that were radiatively coupled into the receiver at the audio module from the ribbon cable carrying the FPGA digital control signals were

eliminated. Currently, the FPGA and DDS are housed in a separate box while the audio module has been moved in the box containing the receiver components in the RF section in close proximity to the mixers. The module is placed within a small shielding metal box. All FPGA signals carrying digital logic have been converted to coax cables.

(iii) A calibration loop consisting of a BAW delay line with a nominal delay of 2 μs was integrated into the radar hardware.

(iv) A new and robust FPGA design for radar control signal generation based on synchronous counters was developed, thereby eliminating existing synchronization problems.

(v) A cancellation loop for transmitter leakage cancellation, consisting of an analog output PD2-AO-16/16 card and RF vector modulator, was integrated into the system and its performance tested. Currently, the cancellation is not automated. The best gain and phase values for the vector modulator are manually searched for. This requires the presence of an oscilloscope and spectrum analyzer at the deployment site. Noise from the control signal lines of the vector modulator coupled into the receiver and degraded the radar sensitivity. Simple solution to this problem, utilizing a voltage divider, was proposed and tested. The current design stage and performance of the cancellation loop, and the need of a new design for the IF section, suggest that some of the RF gain can be moved down to the IF section, thus eliminating the need of the existing cancellation loop.

(vi) The IF receiver gain was increased. More gain was required in the receiver in order to bring the desired signal level above the data acquisition quantization noise floor. Two of the three available 40 dB audio amplifiers were cascaded such that the atmospheric echoes fit in the dynamic range of the data acquisition card

(vii) New audio filters were designed and implemented. The steep frequency response of the AVENS audio filter created filter ringing which after the additional audio section gain was saturating the data acquisition. A new IF filter consisting of a high pass and low pass filter cascade was designed and integrated into the hardware. The new filter characteristics were chosen such that it effectively cancels the transmit leakage while allowing for observation of low altitudes, and has ringing that does not saturate the data acquisition.

After integration and/or modification of the different radar blocks, they were tested in laboratory conditions to evaluate their performance and compare it with the expected ideal performance. Laboratory tests involved the following.

(i) The transmit power was measured. It was confirmed that the radar outputs the desired power of 30 W.

(ii) The gain of the RF section (before mixer) and the IF section was measured and recorded to be 39.5 dB and 80 dB, respectively.

(iii) The new IF filter frequency response was measured and its performance was confirmed to match with the expected values.

(iv) Noise figure measurements were conducted using the gain and Y-factor method. The noise figure was measured to be 1.31 dB with the gain method and 1.42 dB with the Y-factor method for the center frequency of 915 MHz. Results were in very good agreement with the theoritically calculated value of 1.28 dB. The radar noise floor was measured and found to be 8 dB higher than the calculated value. The source of that excess noise was found to be the internal noise of the cascaded audio amplifier pair.

(v) The calibration loop performance was analyzed and tested and the results were used to determine the true available SNR of the Wind Profiler.

(vi) Limitations of the cancellation loop were discussed and transmit leakage cancellation tests were conducted, and the results recorded. The radar noise floor increased by about 22 dB when cancellation was attempted. The reason for that was the noisy control signals of the vector modulator which coupled into the canceling signal and from there into the receiver chain. Efforts were made to alleviate the level of noise thus coupled. The achieved reduction of noise coupling was about 17 dB. Solutions were proposed for further improvement of that value.

The Wind Profiler performance was tested during a few field deployments. The first deployment was at the UMASS horse farm and the acquired data suggested that the received signal was strongly clutter contaminated due to insufficient antenna back and sidelobe levels. The available SNR was reduced as attenuation needed to be added in the receiver chain (the noise floor is constant and set by the audio amplifier module) making the radar insensitive to atmospheric refractive index fluctuations backscatter. The cancellation loop was also tested and the maximum achieve cancellation was around 10 dB. The radar was moved to Tilson farm where shrouds around the antennas were built to prevent energy spill over through the antenna backlobe. The clutter rejection didn't improve significantly which suggested that sidelobes were the primary path for strong target clutter entering into the receiver. The Wind Profiler sensitivity was tested during rainfall. The reflectivity factor was estimated with the available data and found to be in good agreement with the base reflectivity provided by the National Weather Service archive. This experiment confirmed the expected radar sensitivity and antenna alignment in terms of look direction and polarization. However, in its current configuration the radar is incapable of sensing the weak atmospheric refractive index fluctuations.

6.2 Recommendations for Future Work

The Wind Profiler system has undergone important hardware transformations and upgrade. There still exist error sources and system imperfections that prevent it from reaching its desired ideal performance. They were all well identified, and eliminated as time permitted during the laboratory testing and the field deployments, and are described in the main body of this thesis. The following section tries to deliver the insight and knowledge gained during the research and summarize the recommendations for future work that rise from it.

The major error sources include (i) the raise in the radar noise floor due to the internal noise of the audio amplifier module, (ii) the additional noise introduced into the received from the noisy vector modulator control lines, and (iii) the strong clutter entering the receiver through the antenna sidelobes.

The low transmit power and the low antenna gain require a receiver with low noise and a very high gain. The internal noise of the audio amplifiers used in the IF section becomes significant due to the high IF gain. That brings the need for a new audio amplifier module. Currently, an ultra low noise operational audio amplifier is being design for that purpose. Part of the gain in the RF section will be moved down to the IF section thus eliminating the need for cancellation loop in most deployment conditions. Simulations will be performed to determine the best possible IF filter response allowing for low altitude observation of the nocturnal boundary layer.

During the field deployments is was observed that the sidelobe level of the currenly used Wind Profiler antennas is insufficient and brings the need for attenuation to be added in the receiver chain in order to prevent the data acquisition from saturation. The shroud fence that was built is about 20 cm higher than the antennas and doesn't improve the sidelobe levels significantly. A higher shroud fence needs to be built for that purpose. A shroud fence can also be built directly on the truck bed keeping the system mobile.

In a future radar system, where a similar cancellation loop is needed, caution should be taken to guarantee that noise does not couple into the receiver. The suggestions in Section 4.5 can be used as guidelines for improving the cancellation loop noise performance.

BIBLIOGRAPHY

[1] Agilent Technology, Inc. *Noise Figure Measurements Personality Guide*. Agilent Technology, Inc., USA, 2006.

[2] Albert Genis. UHF FMCW wind profiler. *Master Thesis, Universitat Politecnica de Catalunya* (May 2008).

[3] Briggs, B. H., Phillips, G. J., and Shinn, D. H. The analysis of observations onspaced receivers of the fading of radio signals. *Proc. Phys. Soc. London Sect. B 63* (1950), 106–121.

[4] Burrows, C. R., and Attwood, S. S. Radio Wave Propagation, consolidated summary technical report of the committee on propagation, NDRC. *Academic Press, New York* (1949), 219.

[5] Chadwick, Moran, Strauch, Morrison, and Campbell. A New Rarar For Measuring Winds. *American Meteorological Society 57*, 9 (September 1976), 1120–1125.

[6] Chadwick, R.B., and Moran, K.P. Long term measurements of c_n^2 in the boundary layer. *Radio Science 15*, 2 (March-April 1980), 355–361.

[7] Christopher L. Hollaway, Richard J. Doviak, Stephen A. Cohn, Richard J. Lataitis, and Joel Van Baelen. Cross correlations and cross spetra for spaced antenna wind profilers 1. Theoretical Analysis. *Radio Science 31*, 1 (January-February 1996), 157–180.

[8] David Atlas. *Radar in Metrology*. American Meteorological Society, Boston, 1990.

[9] Marshall, J. S., Langille, R. C., and McK. Palmer, W. Measurement of rainfall by radar. *Journal of Atmospheric Sciences 4*, 6 (December, 1947), 186–192.

[10] Merrill Skolnik. *Radar Handbook*. McGraw - Hill, Boston, Massachusetts, 1990.

[11] Muschinski, A., Volker Lehmann, Lutz Justen, and Gerd Teschke. Advanced radar wind profiling. *Meteorologische Zeitschrift 14*, 5 (October 2005), 609–625.

[12] Ottersten H. Atmospheric structure and radar backscattering in clear air. *Radio Science 4*, 12 (1969), 1179–1193.

[13] R. Gunn, G. D. Kinzer. The terminal velocity of fall for water droplets in stagnant air. *Journal of Atmospheric Sciences 6*, 4 (1949), 243–248.

[14] Richard J. Doviak, and Dusan S. Zrnic. *Doppler Radar and Weather Observations*. Dover Publications, Inc., Mineola, New York, 1984.

[15] Richter J. H. High resolution tropospheric radar sounding. *Radio Science 4*, 12 (1996), 2061–2068.

[16] Stephen A. Cohn, Christopher L. Hollaway, Steven P. Oncley, Richard J. Doviak, and Richard J. Lataitis. Validation of the UHF spaced antenna wind profiler for heigh-resolution boundary layer observations. *Radio Science 32*, 3 (May-June 1997), 1279–1296.

[17] Strauch, R. J., Merritt, D. A., Moran, K. P., Earnshaw, K. B., and Van De Kamp, D. The Colorado Wind-Profiling Network. *Journal of Atmospheric and Oceanic Technology 1* (1984), 37–49.

[18] Tatarski, V. I. *Wave Propagation in a Turbulent Medium*. McGraw - Hill Book Company, Inc., New York, New York, 1961.

[19] Turker, Frasier, S., Muschinski, A., and Pazmany, A. An s-band fmcw boundary layer profiler: Description and initial results. *Radio Sience 38*, 4 (2003).

[20] Turker Ince. Cleai-air radar observations of the atmospheric boundary layer. *UMASS Ph.D Dissertation* (May 2001).

[21] Zakharov, V. E., L'Vov, V. S., and Falkovich, G. *Kolmogorov Spectra of Turbulence I: Wave Turbulence*. Springer - Verlag, New York, New York, July 1992.